UNIVERSITY OF OKLAHOMA

GRADUATE COLLEGE

DIAMOND AND PARYLENE COMPOSITE BONDING: A POWERFUL METHOD FOR ELECTRONIC THIN FILM DEVICE FABRICATION

A THESIS

SUBMITTED TO THE GRADUATE FACULTY

in partial fulfillment of the requirements for the

Degree of

MASTER OF SCIENCE

By

XINGHUA SHI
Norman, Oklahoma
2016

DIAMOND AND PARYLENE COMPOSITE BONDING: A POWERFUL METHOD FOR ELECTRONIC THIN FILM DEVICE FABRICATION

A THESIS APPROVED FOR THE
SCHOOL OF ELECTRICAL AND COMPUTER ENGINEERING

BY

_____
Dr. Patrick McCann, Chair

_____
Dr. Zhisheng Shi

_____
Dr. Hjalti Sigmarsson

Acknowledgements

First of all, I would like to express my sincere gratitude to my supervisor, Dr. Patrick McCann, for his guidance, enthusiasm and support throughout this research. I am also deeply grateful of his suggestions and comments in completion of this thesis. To my committees, Dr. Zhisheng Shi and Dr. Hjalti Sigmarsson, I am grateful for your assistance and instructions during my study and thesis.

Furthermore, I would like to thank Dr. Zhihua Cai, Dr. Khosrow Namjou, Dr. Ghulam Hasnain, Dr. Lihua Zhao, Mr. Creighton Hawkins, Mr. Dejan Nedin, Mr. Leonard Olona and Dr. Binbin Weng for their discussion, help and their invaluable advice during my research work.

I greatly acknowledge Dr. Preston Larson in Samuel Roberts Noble Microscopy Laboratory for SEM images in addition to his invaluable time in training me.

I would also like to thank all my beloved family. Without their love, understanding and support, I could not have finished this thesis.

Table of Contents

List of Tables

List of Figures

Abstract

A new and powerful method for electronic device fabrication is presented. A diamond and parylene composite thin film layer bonding process is described. Two sizes of diamond particles, nominally 0~0.5μm and 0~2μm were used to form different composite bonding layers. Scanning electron microscopy (SEM) images show good bonding quality with no observed voids within the approximately 10 micron thickness of the bonding layer and along about 1 cm of bonded length. In addition, a thin film IV-VI semiconductor material grown by molecular beam epitaxy (MBE) was used to perform thermal conductivity measurements. The technique involved flip chip bonding the IV-VI epitaxial layer to one side of two silicon chips bonded together with the parylene composite film, attaching the other side of silicon chip assembly to a heat sink, and measuring the blue shift in the photoluminescence (PL) emission from the IV-VI epitaxial layer while being illuminated (and heated) with a diode laser. The PL data provided an accurate temperature measurement of the laser-heated surface. This measurement procedure accurately simulates the use of a parylene/diamond composited material in the packaging of high power electronic devices. The amount of heating with a parylene/diamond composite bonding material was 19.5℃, which was significantly lower than the 36.3℃ observed for a control sample that was parylene bonded without diamond. These results clearly show that incorporation of diamond particles in parylene can significantly reduce hot spot temperatures in electronic devices. Finite element thermal modeling was used to determine the thermal conductivity of the parylene/diamond composite material using the hot spot temperatures obtained from the PL measurements as boundary conditions. Modeling results showed an improvement

factor of 3.6 with incorporation of diamond. This corresponds to a thermal conductivity increase from 0.083 W/mK for bulk parylene to 0.30 W/mK for the parylene/diamond composite material. Moreover, the ability to from a thin bond with a thickness of 10 microns or less provides additional thermal management benefits over other device packaging techniques that involve much thicker bonding layers. Two conclusions can be drawn from this work. The first is that a proof-of-concept has been established for the opportunity to develop an improved electronic device packaging material based on thin film parylene/diamond composites. The second is that thermal conductivities of experimental thin film materials for thermal management applications can be obtained by using photoluminescence measurements of IV-VI semiconductor thin films to determine the boundary conditions for finite element thermal modeling analysis. Continued work using this new method for measuring thin film thermal conductivity and further refinement of parylene/diamond composite materials should result in a new class of electrically insulting materials that can be used to improve the thermal management of high power electronic devices.

Chapter 1: Introduction

The world's energy supply should be reliable, diverse, and affordable. Sustainable and hybrid energy supply development has been a significant cornerstone for the next industrial revolution even though fossil fuels are currently the primary energy source in the world. However, environmental impacts with fossil fuel use cannot be neglected. The other concern with fossil fuel usage is waste heat generation which reduces energy efficiency. To recover waste heat energy thermoelectric and thermophotovoltaic devices are promising options because they can transfer heat flow and thermal radiation into useful electrical energy. For those advanced device applications, electronic component fabrication and thermal management are important issues for development of high performance systems. This thesis introduces a new solution for electronic component packaging. Its further development and adoption by industry can satisfy the thermal management requirements of existing and future electronic devices for sustainable energy applications.

Thermal Management and Heat Dissipation

Thermal dissipation at the active region of electronic devices is a fundamental process of considerable importance. Inadequate heat dissipation can lead to prohibitively large temperature rises that degrade performance. [1-5] Figure 1 shows steam carrying heat away from a Google data center, a necessity for all data centers where computer systems need to remain cool. In electronics systems, such as printed circuit boards with multiple electronic components, heat is generated by the components in use, and it is necessary to remove or dissipate heat to prevent over heating which could result in break-down of one or more of the components [6-7].

Figure 1 Steam carries heat away from Google's data center in The Dallas, Oregon [5]

Various previous approaches to thermal management of integrated circuits (ICs) have drawbacks that limit their application, incur significant additional costs, and/or impose undesirable restrictions on circuit lay-out and design. Therefore, it would be desirable if a circuit construction technology were available that provided improved thermal management for high power ICs and discrete components. Flip chip packaging is one such technology. It enables thermal enhancement of localized areas of the circuit or device, it can lower cost, allow greater design flexibility, is compatible with leaded components, and it permits mounting of two heat sinks on both sides of the circuit or device component.[7] Metals, which are good conductors of heat and electricity, have been traditionally used for flip chip packaging. Table 1 lists the materials properties of some selected metals and alloys used in electronic packaging. [8]

Table 1. Materials properties of some selected metals and alloys used in electronic packaging

Metals and alloys	Thermal conductivity at 0-100° C	Electrical Resistivity At 20° C	Thermal expansion (1/K×10^6)	Density (20° C) (g/cm^3)	Melting point (° C)
Aluminum (Al)	238	2.7	23.5	2.7	660
Al 2024-T4	121	5.82	23.2	2.78	502-638
Al 5052-H32	138	4.99	23.8	2.68	607.2-649
Al 6061-T4	154	4.32	23.6	2.71	582-651.7
Al 7075-T6	130	5.15	23.6	2.81	477-635
Antimony(Sb)	17.6	42.0	8.11	6.7	630
Beryllium (Be)	167	5.0	12.0	1.8	1,284
BeCu (C17200)	105	7.68	17.5	8.36	871-982
BeCu (C17510)	245	3.79	17.6	8.82	1029-1068
Bismuth (Bi)	7.9	116	13.4	9.8	271
Cadmium (Cd)	92.0	7.4	31	8.6	321
Chromium (Cr)	69.0	13.0	6.5	7.2	1,875
Copper (Cu)	393	1.7	17.0	8.9	1,491
Red brass(15%Zn)	151	4.66	18.7	8.8	990-1025
Yellow brass(35%Zn)	119	6.38	20.3	8.8	905-930
Phosphor Bronze (C5210)	63	13.0	18.0	8.8	880-1030
Cu-Ni-Sn(C72700)	50	14.0	17.1	8.88	1020-1110
Germanium(Ge)	59.0	>10^6	5.8	5.3	937
Gold(Au)	263	2.3	5.8	19.3	1,064
Indium (In)	81.9	9.1	25.0	7.3	156
Iron (Fe)	1.0	9.7	6.8	7.9	1,525
Invar (64%Fe–35%Ni)	13.8	82	1.3	8.13	1,427
Kovar (54%Fe–29% Ni–17%Co)	16.3	49	5.1-5.5	7.85	
		1,450			
Steel 1015	51.9				
Stainless Steel 301	16.2	15.9	11.9	7.87	
Lead(Pb)	34.3	72	16.6	8.03	1399-1421
Lithium (Li)	71.1	21.0	20.0	11.7	328
Magnesium (Mg)	167	9.4	55.0	0.5	179
Mg–Al (AZ31)	96	4.0	26.0	1.7	650
		9.2	26.0	1.77	605-630
Molybdenum(Mo)	142	5.6	5.2	10.2	2,595

Nickel(Ni)	88.0	6.8	13.4	8.9	1,254
Nichrome (80%Ni-20%Cr)	13.4	108	14.0	8.4	1,400
Ni-Cu(N04400)	21.8	54.7	13.9	8.8	1300-1350
Palladium(Pd)	71.0	10.9	10.9	12.0	1,550
Platinum(Pt)	71.0	10.7	9.1	21.5	1,770
Rhodium (Rh)	84.0	4.7	8.4	12.4	1,959
Silicon (Si)	83.0	$>10^{10}$	7.5	2.3	1,414
Silver (Ag)	418.0	1.6	19.0	10.5	961
Tantalum (Ta)	54.0	14.0	6.5	17.0	2,985
Tin (Sn)	65.0	12.9	12.0	7.3	232
Titanium (Ti)	17.0	55.0	8.9	4.5	1,670
Ti–6Al–4V	6.7	178.0	8.6	4.4	1604-1660
Tungsten (W)	165	6.0	4.5	19.4	3,380
Zinc (Zn)	111	26.0	30.0	7.1	420
Zirconium (Zr)	20.0	45.0	5.9	6.5	1,860

Development of compact and cheap-to-fabricate heat sinks for electronic devices is both a major challenge and a solution for enabling the reliable operation of high power electronic devices. The peak power density of electronic devices is typically limited by heat transfer at the device, substrate, package, and system levels (chip-level, board-level and system level). Much progress has been made in the past decade on improving thermal management of power semiconductor devices. However, there remain significant opportunities for improvement associated with technologies such as high power semiconductor lasers and radar amplifiers that are still severely limited by ineffective cooling. [3] To ensure that heat flows from the electronic components to the heat sink, a heat transfer medium is typically interposed between the components and the heat sink, since it would otherwise be difficult to ensure proper contact between the electronic components and the heat sink. One type of heat transfer medium used has been non-electrically conductive matrix resin. Because of the risk of a short circuit in an

electronic system if the heat transfer medium is electrically conductive, non-electrically conductive media, have been applied. However, non-electrically conductive media are typically relatively poor thermal conductors. Accordingly, it would be desirable to achieve better thermal conductivity between electronic components and an electronically-isolated heat sink. [6]

The need for advanced thermal management materials in electronic packaging has been widely recognized as thermal challenges became barriers to the electronic industry's ability to provide continued improvements in device and system performance. With increased performance requirements for smaller, more capable, and more efficient electronic power devices, systems ranging from active electronically scanned radar arrays to web servers all require components that can dissipate heat efficiently. This requires that the materials have a high capability for dissipating heat and maintaining compatibility with the die and electronic packaging. In response to these critical needs, revolutionary advances in thermal management materials and technologies for active and passive cooling now promise cost-effective thermal management solutions. In response to critical needs, there have been revolutionary advances in thermal management materials, such as tailored coefficient of thermal expansion, low-density materials with thermal conductivities ranging between 400 and 1,700 W/mK. Some are low cost; others have the potential to be low cost in high-volume. [9] Production applications include motor controller, aircraft and spacecraft microwave, and power supply subsystems, servers, laptops, printed-circuit boards, printed-circuit board cold plates/heat spreaders, cellular telephone base stations, hybrid electric vehicles, power modules, phased array antennas, thermal interface materials, optoelectronic

telecommunication packages, laser diode and LED packages, and plasma displays[10]. As shown in Table 2 [9], among the advanced materials, high performance composite materials provide great advantages over conventional materials for electronic packaging. Some of these materials have extremely high thermal conductivities (more than twice that of copper); low tailorable coefficients of thermal expansion; offer weight savings of up to 80%; have extremely high strength and stiffness; are low-cost, and can benefit from near net-shape fabrication processes. In addition, the large design space available with composites can provide even greater benefits with continuous development. Novel composite materials have been developed that provide unique combinations of properties that make them outstanding candidates for packaging and thermal management applications.

Table 2 Physical properties of advanced thermally conductive materials

Base material (matrix)	Reinforcement Type	Vol%	Thermal Conductivity (W/mK)	Thermal expansion (1/K×10^{-6})	Electrical resistivity (Ω cm)	Density (g/cm^3)
Diamond	-	0	900-2,320	1.0-1.5	10^{13}-10^{16}	3.52
Carbon fiber	-	0	100-500	4-5(L) -1(T)	0.00155	1.81
Carbon nanotubes	-	0	6,600	-1.0	10^{-4}	2.0
Vapor grown carbon fibers	-	0	1200-1950	-1.0	10^{-4}	1.8-2.0
Carbon	VGCF	70	910	-	-	1.8-2.0
Epoxy	Carbon fiber	60	310(X,Y)	-1.1	-	1.85
Epoxy	VGCF	73	660	-	-	1.87
SiC	VGCF	20	310	-	-	2.9
SiC	Diamond		500	-	-	3.1-3.3
Copper	Diamond	50	420	5.5	-	5.35
Copper	Carbon fiber	28	290(X,Y)	6.5	-	7.2
Copper	CNTs	50	1,024	-	-	5.45
Copper	VGCNF	50	840	5.5	-	5.45
Copper	Carbon particles	50	150-300	8.0-9.0	-	5.9
Aluminum	VGCF	37	642	5.0	-	2.44
Aluminum	Carbon Whisker	40	230	4.0	-	2.40
Aluminum	SiC particles	60	180	9.0-10	-	2.9
Aluminum	Graphite particles	50-70	190-270	6.5-9.5	-	2.2-2.0

.

The importance of effective heat conduction has motivated the development of a composite layer containing high-thermal-conductivity diamond. Having a high thermal conductivity [up to 2,200 W/ (mK)], diamond occupies a prominent place among thermal management materials. It offers promise for developing high-efficiency heat sinks for semiconductor lasers, high-frequency, high power transistors, optical

amplifiers, power LEDs, integrated circuits, etc. [11] Furthermore, thermally conductive polymer matrix composites have been increasingly used for thermal management of electronic packaging systems. The polymer matrices for thermally conductive composites shall preferably exhibit low dielectric constant, low dissipation factor, low coefficient of thermal expansion, and compatibility electronic packaging applications. [9]

The aggressive ongoing microminiaturization of electronic components is creating an urgent need for innovative cooling schemes to maintain chip temperatures below limits set by both materials and device reliability. Initial efforts focused on fan-cooled heat sink attachments. But as heat dissipation rates continue to escalate, interest is shifting to dielectric liquid coolants using a variety of single-phase cooling schemes. Figure 2 compares the heat transfer coefficient in these traditional methods. [12]

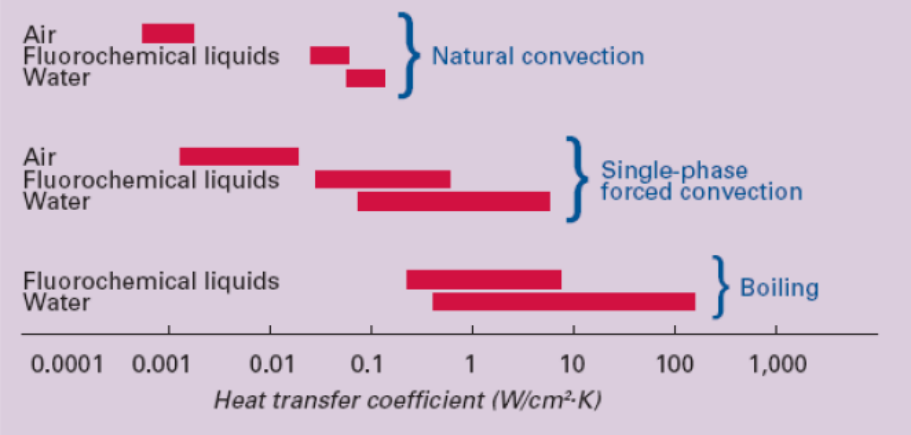

Figure 2 Normal heat transfer ranges [13]

Furthermore, heat dissipation challenges are not limited to computer chips. Similar challenges have emerged with devices found in numerous medical, transportation, energy, aerospace, and defense applications. These applications spurred intense new research efforts in pursuit of high performance cooling solutions. [12] Figure 3 and

Figure 4 show the spray cooling schemes and heat transfer cooling coefficient data for various approaches.

In summary, cooling system design and thermal interface materials are the key technical issues to consider in a heat dissipation study.

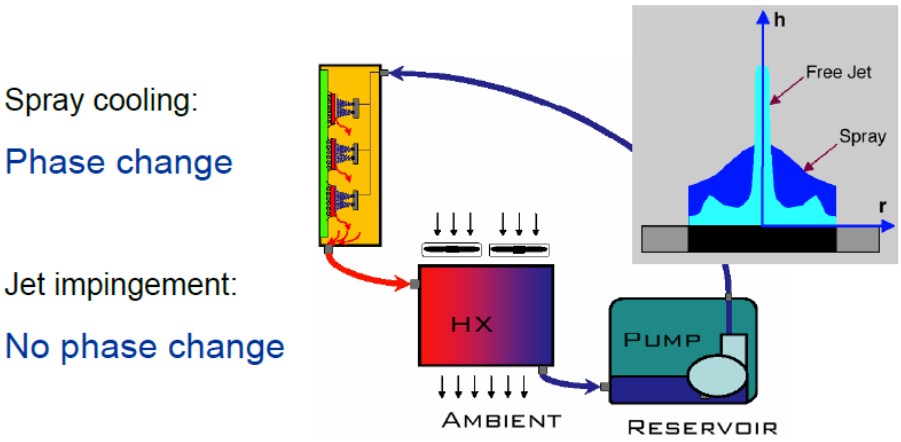

Figure 3 Jet Impingement-Spray Cooling [13]

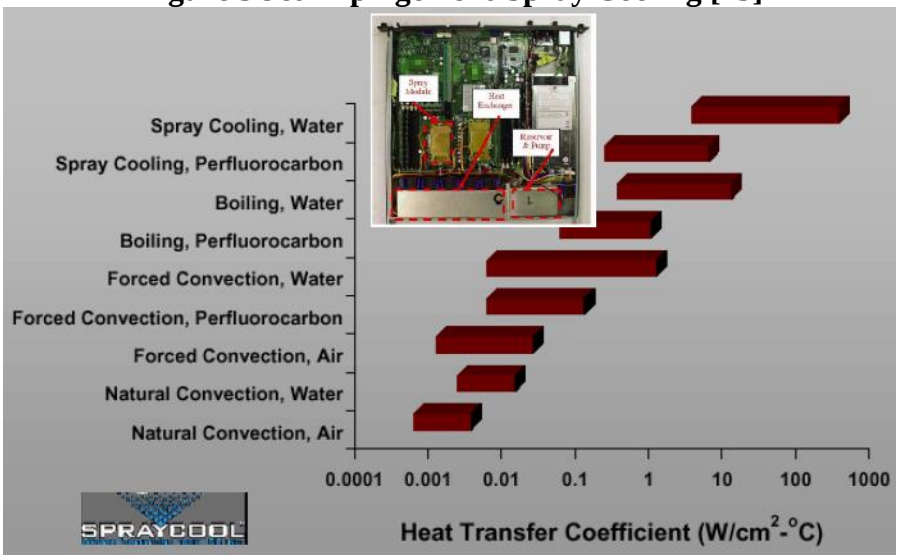

Figure 4 Heat transfer on Spray Cooling [13]

Thermal Conductivity and Mean Free Path Spectrum

Spectral phonon mean free path, phonon group velocity and spectral phonon relaxation times determine the thermal properties of numerous novel materials. Thermal conductivity is the property of a material that indicates its ability to conduct heat.

$$K = \frac{n<v>\lambda c_V}{3N_A} \qquad (1)$$

In Equation (1) K is thermal conductivity, n is the particles per unit volume, v is mean particle speed, λ is the mean free path, c_V is the molar heat capacity and N_A Avogadro's number. Spectral phonon mean free path, determined by phonon scattering rate, dominates the behavior of thermal properties, especially the thermal conductivity K.

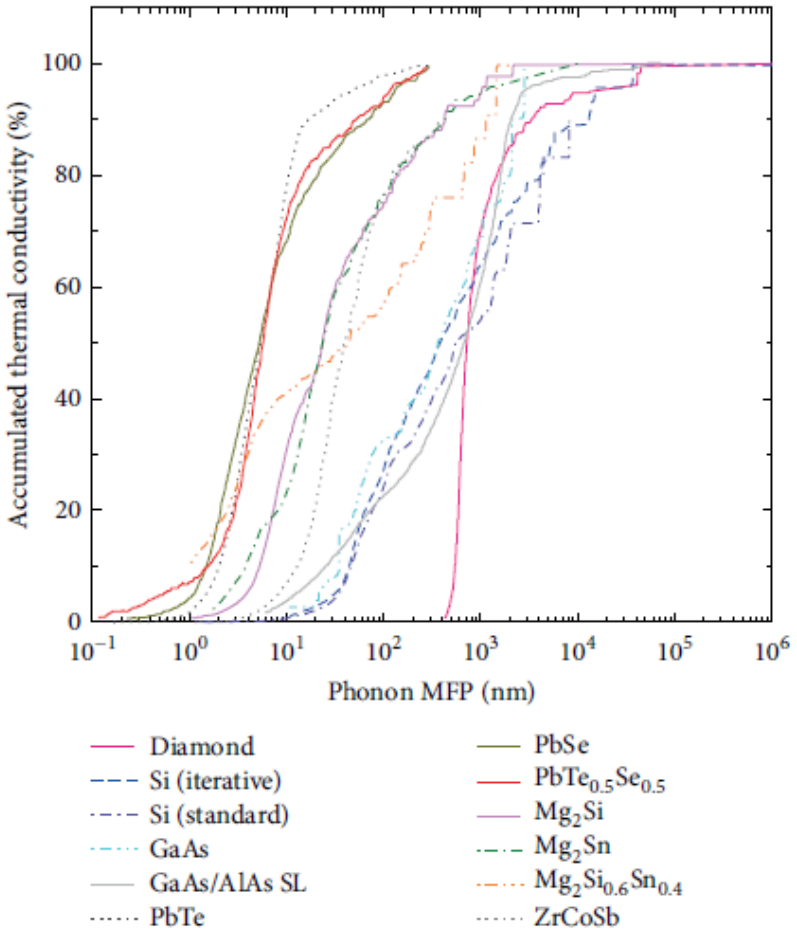

Figure 5 The accumulated thermal conductivity of different bulk materials as a function of phonon mean free path at room temperature calculated from anharmonic lattice dynamics methods by first principle approach [14]

Based on the Boltzmann transport equation under the relaxation time approximation, thermal conductivity is determined by the spectral phonon relaxation time τ_λ, phonon group velocity v_λ, and phonon specific heat c_λ [15]

$$K_z = \frac{1}{V}\sum_\lambda (v_\lambda \cdot \hat{z})^2 c_\lambda \tau_\lambda \qquad (2)$$

Where $\hat{z}$ denotes the transport direction, λ is the shorthand of phonon mode (**k,** υ) with **k** representing the phonon wave vector and υ labeling phonon dispersion branch, V

is the volume of the domain, and the summation is done over the resolvable phonon modes in the domain.

The third-order anharmonic lattice dynamics calculation is a more accurate method which can predict the intrinsic spectral phonon relaxation times, was introduced by Maradudin and the collaborators [16, 17]. Motivated by the question of which phonons with what kind of mean free path contributed the most to the total thermal conductivity, the cumulative *k*'s as functions of phonon mean free path are calculated by an anharmonic lattice dynamics method with first principle approach as shown in Figure 5. Thermal transport in diamond is dominated by the phonon with a narrow range of mean free path (0.4-2 μm). In diamond, phonons with 500 nm < l < 3.5 μm account for 80% of heat transport. [18] Alternatively, PbTe-PbSe alloys with nanoparticle sizes below 10 nm are found to have as much as a 60% reduction to the thermal conductivity as compared to binary PbTe or PbSe bulk material.

According to theoretical calculations [19] and experimental results, the use of larger particles can lead to improved thermal conductivity of composite materials by forming thicker conductive paths thus reducing the interfacial phonon scattering effect between matrix and fillers. Table 3 shows an increased thermal conductivity for a composite material with larger diameter AlN particles. AlN (A-100) particle diameter is 4 μm and AlN (A-500) particle diameter is 20-25 μm. [20] As shown in Figure 6 when the diamond particle diameter is increased from 25 μm to 100 μm, the composite thermal conductivity is increased from about 600 W/mK to 800W/mK.

Table 3 Thermal conductivity of polymer composites with different types of single filler [19]

Filler	Filler (vol%)	Thermal conductivity (W/mK)
AlN(A-100)	0	0.35
	10	0.46
	30	0.75
	50	1.08
	60	2.01
	70	2.31
	75	2.27
AlN(A-100) treated	60	2.14
AlN(A-500)	60	2.42
BN	50	3.66

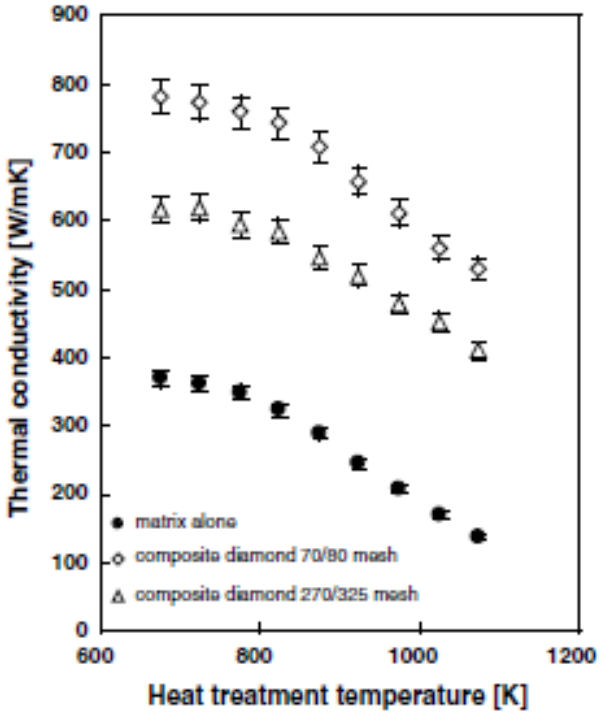

Figure 6 Thermal conductivity of Ag matrix and the two composites with diamond particles of 25 and 100μm radius as a function of heat treatment temperature between 673 and 1073K [21]

Measurement of thin film thermal conductivity

The thermal properties of thin films and superlattice materials have attracted significant interest due to their potential applications in thermal management and thermoelectric

device design. Thermal conductivity of thin films can be measured with different techniques. One method is the 3-ω method [22-26], a modulated and time resolved thermo-reflectance technique [27-28]. Other steady-state and transient techniques have also been developed [29-34].

Currently the 3ω method is one of the most widely used because of its low cost, simplicity and high accuracy. The 3ω method, which uses a metal microbridge deposited on thin film samples as both an electrical-heater and a temperature sensor, has become a very effective technique for measuring the thermal properties of dielectric thin films. Figure 7 and 8 describe the 3ω method. However, applications of the 3ω method to electrically conducting or semiconducting materials can be challenging in sample preparation. [35] Usually a typical frequency range from 5Hz to 200 kHZ is applied for the 3ω method. [26,36] Using a typical thermal diffusivity value $\alpha = 3\times10^{-6}$ m^2/s, the thermal penetration depth d can be several to hundreds of microns from the relationship of $L=\sqrt{\alpha/(\pi f)}$. [26] As a result, such a quasisteady-state method is insensitive to the interface thermal conductance, and cannot be used to measure accurately the thermal conductivity of nanoscale thin films. [28]

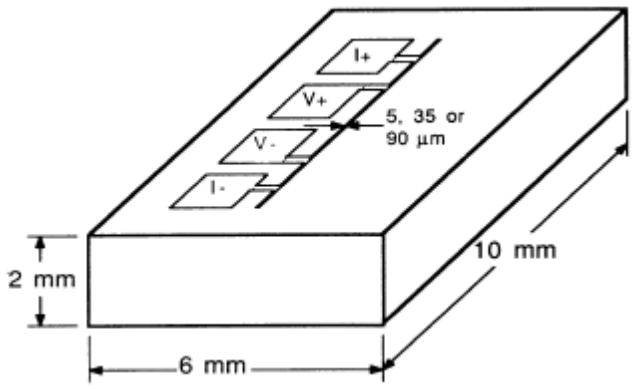

Figure 7 Evaporated metal patterns produced on the face of a 3ω method sample. The four pads are the connections for current leads I+, I and voltage leads, V+, V.

The narrow metal line that serves as the heater and thermometer for the measurement of the thermal conductivity is at the center of the face of the sample. Pattern made by photolithography (line widths 5 or 35 pm) or by evaporation through a mask (line width 90 pm). [22]

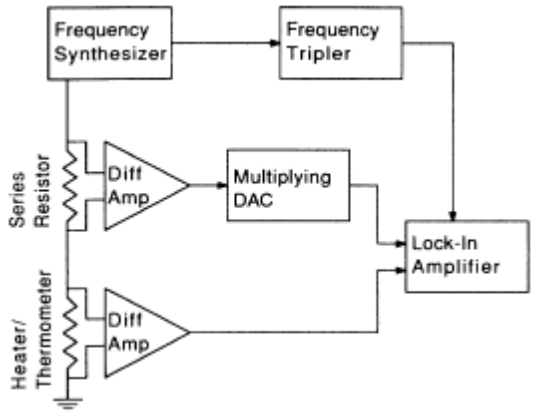

Figure 8 Schematic diagram of the equipment used for thermal conductivity measurements using the 3ω method. [37]

Ultrafast thermoreflectance techniques often employ subpicosecond lasers. Repeated laser pulses are divided into two beams. The pump beam excites a sample and the probe beam measures the changes in the reflectivity or diffraction, which is temperature-dependent. The imperfections in the stage motion, the overlap of pump-and-probe pulses, and the divergence of the delayed optical beam could all introduce measurement errors. [38-40] However, the optical alignment involving a moving stage is still rather tedious. [28] Figure 9 outlines the thermoreflectance method for thermal conductivity measurements.

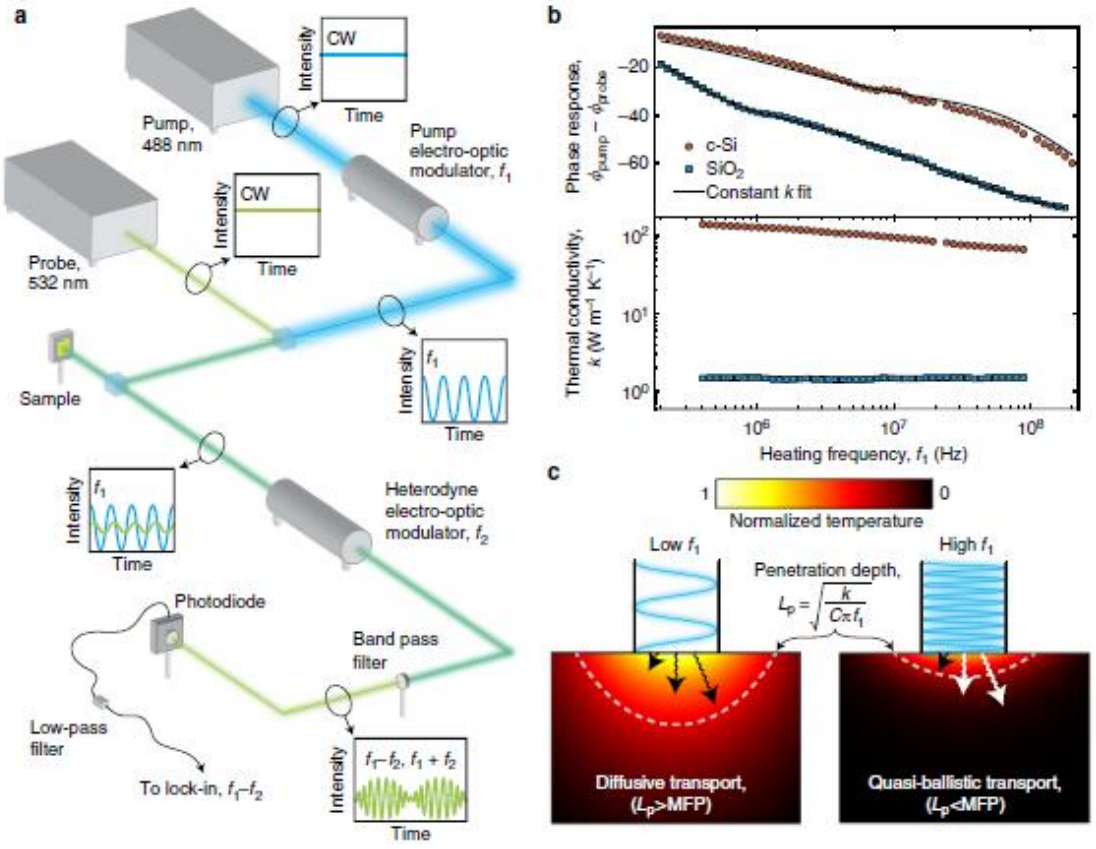

Figure 9 Broad-band experiments reveal a heating frequency-dependent thermal conductivity. [41]

Recently, a novel thin film thermal conductivity measurement method that takes advantage of radiative interband transitions in IV-VI semiconductors has been developed [42-44]. Mid-infrared photoluminescence emission is measured when the sample surface is exposed to continuous wave laser illumination. The continuous wave laser heats the sample surface, and this causes a blue shift in the photoluminescence emission energy, which corresponds to lattice temperature rise of the sample surface. It is therefore possible to measure the temperature gradient through the thin film when the substrate backside is thermally anchored to a temperature-stabilized heat sink. As with other thermal conductivity measurement techniques, finite element analysis (FEA) is

used to extract the thermal conductivity [42], but since the measurement is performed under steady state conditions, it more accurately simulates the conditions under which an actual device material would be used in a typical application. [43] Figure 10 is the photoluminescence system block diagram which includes a near-IR power meter, Fourier transform infrared (FTIR) spectrometer and sample mount stage. The solid line represents the near-IR pump laser optical path and the dotted line represents the optical path for photoluminescence emission. Figure 11 shows the blue shift of photoluminescence emission with increased optical power and with increased heatsink temperature from a PbSrSe/PbSe multiple quantum well material.

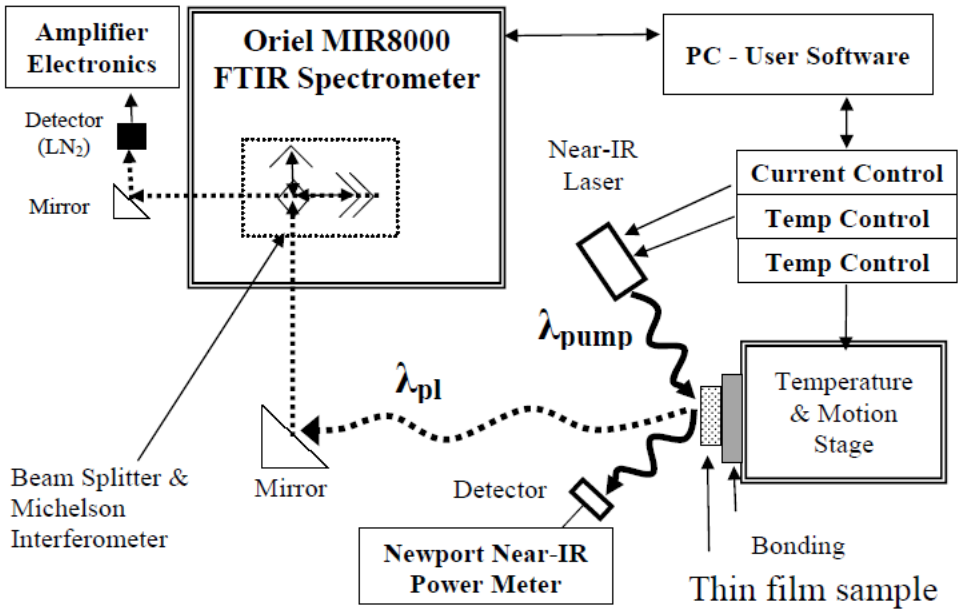

Figure 10 Photoluminescence system block diagram that includes an FTIR, near-IR power meter, and sample mount stage. The solid line represents the Near-IR pump laser optical path and the dotted line represents the optical path for photoluminescence. [44]

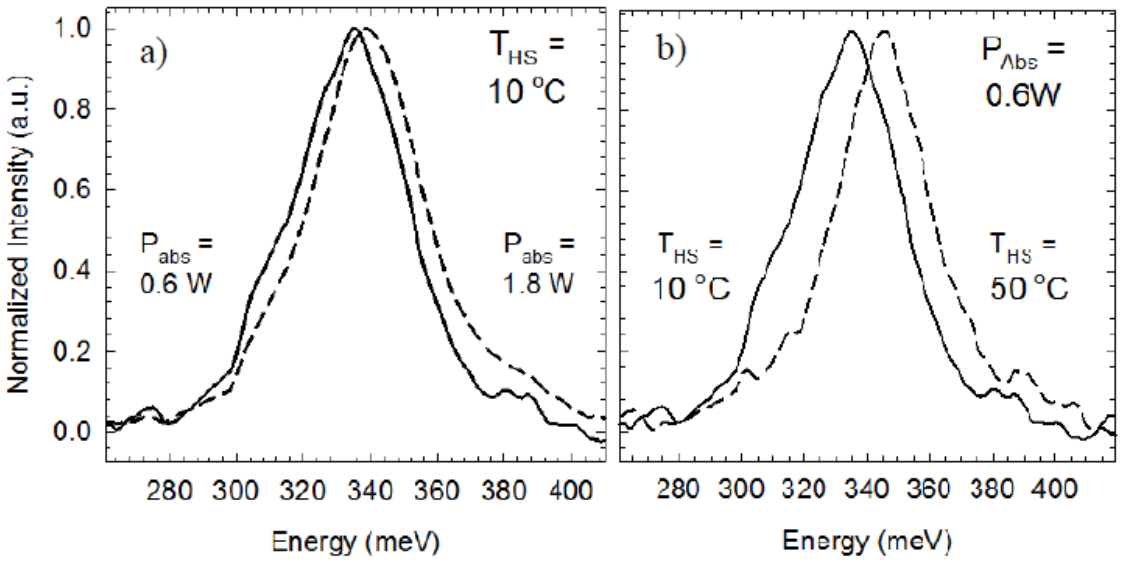

Figure 11 Photoluminescence emission shift for multiple quantum well sample: a) with increased optical pump power absorbed (P_{abs}) at a constant heat sink temperature T_{HS} = 10 ℃ and b) with increased heatsink temperature at a constant P_{abs} = 0.6W. [44]

Thermal Model

Finite element analysis software (Tera Analysis, Toronto, Canada model Quickfield Ver. 5.6) can be applied to calculate the film thermal conductivity. This program creates a periodically spaced mesh of nodes within an accurately scaled film model. To solve the continuous heat conduction problem using a single fixed boundary condition, the heatsink temperature of the film being tested, and a given amount of thermal energy generated within the model. The finite element thermal model used this information to calculate the temperature of each node with temperature of neighboring nodes connected by the mesh lines serving as additional boundary conditions. This model begins with initial guesses for the temperature of each node and then recursively evaluates the phenomenological solution of Fourier's law for thermodynamics, k is the thermal conductivity (W/mK), Q is the heat flux (Watts), T is temperature,

$$\nabla(k \cdot \nabla \mathrm{T}) = -\mathrm{Q} \qquad (3)$$

until the fit error of the model temperature reaches an acceptably low value. [44] For the finite element model the essential boundary conditions are the heat sink temperature and the hot spot temperature, which is determined from the photoluminescence (PL) measurements. With the absorbed power density from the PL pump laser and the dimensions of the sample, the thermal conductivity of a layer between the hot spot and the heat sink can be determined through a trial-and-error fitting algorithm.

Table 4 Heat conduction analysis in finite element model [45]

Heat transfer problem
Temperature (scalar)
Heat flux (vector)
Fixed temperature B.C.
Heat flux B.C.
Internal heat generation
Thermal conductivity

Parylene C Deposition

Parylene is chosen as the dielectric matrix material for this work. It has many attractive properties for electronic device packaging, such as, being lightweight, optically clear,

low cost, chemically insoluble, and having a high dielectric strength. It is also being increasingly used for advanced electronic device and component packaging. Parylene coating is currently used for encapsulating electronic circuitry for automotive applications. Its conformal coating characteristic and pin-hole free deposition improves, solder joint reliability by inhibiting moisture-induced corrosion effects. Parylene coating is also finding additional applications in military and aerospace systems, oil and gas industry, LED lighting and medical devices.

Figure 12 depicts the parylene vacuum deposition process. The parylene coating cycle begins with vaporization of the powdered raw material (dimer), creating a dimeric gas. These dimers are subsequently cleaved to the monomer form in a second stage by heating to 690℃. The active monomer gas is then introduced to an evacuated coating chamber where it disperses and polymerizes spontaneously on the substrate surface at room temperature to form a parylene film.

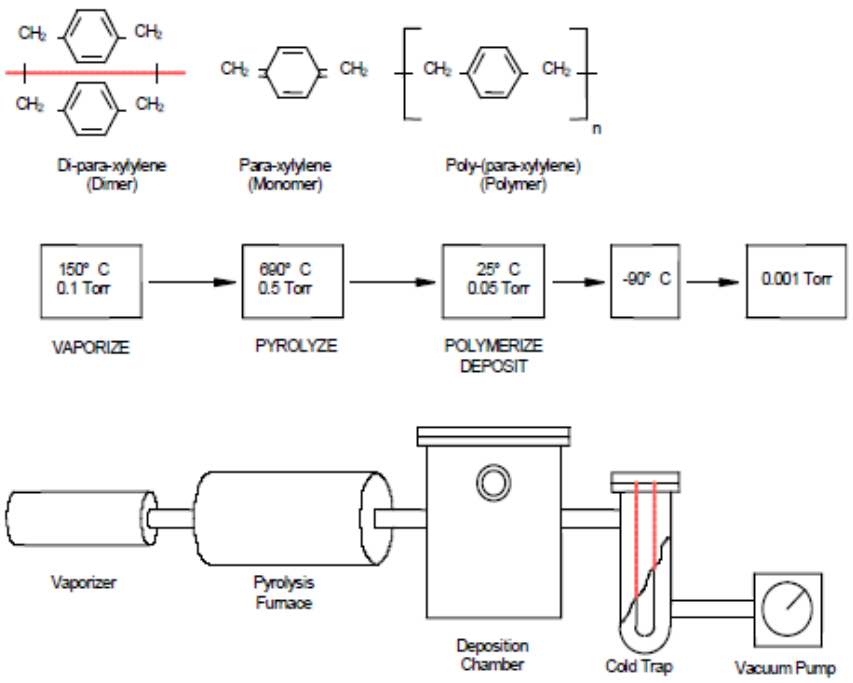

Figure 12 Parylene vacuum deposition process [46]

The requirements for good parylene bonding include reasonable bond strength at a low bonding temperature, bond strength stability over time or after exposure to chemicals, and a low density of voids. Parylene bonding must be performed under 300℃ to protect the polymeric structure. A bond strength more than a few hundred KPa is desirable to hold two microstructures together.

Chemical analysis indicates that no chemical reaction takes place during the heating period of either the parylene film or the powder. Two relevant temperatures are the glass transition temperature (109℃) and the melting temperature (303℃). Thus, the analysis confirmed the hypothesis in Figure 13 that bonding, if possible, between two parylene layers occurs by physical movement of polymer chains, not by their chemical reactions. [47]

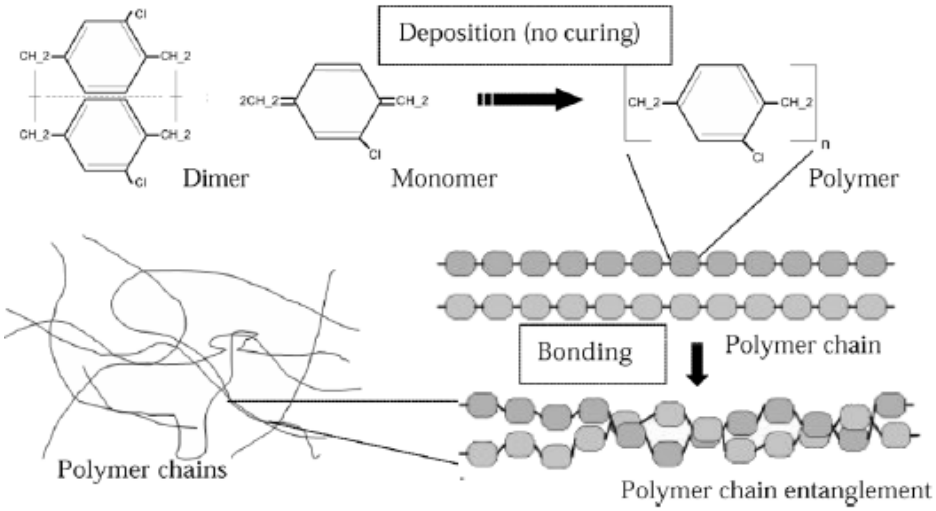

Figure 13 Hypothetical parylene chain entanglements during bonding [47]

Thesis Organization

This thesis will introduce a powerful and new method for thin film device fabrication. The new materials and methods described here can be used to improve high power electronic device heat dissipation when electrically insulating interface layers are needed for device packaging. Chapter two will present results from the characterization of IV-VI semiconductor materials grown by molecular beam epitaxy (MBE). Chapter three will introduce the details of parylene bonding with characterization results that include scanning electron microscopy (SEM), energy dispersive x-ray fluorescence (EDX) and photoluminescence (PL) test results performed using the IV-VI semiconductor material described in Chapter 2. Chapter 3 concludes with finite element thermal modeling results that provide the thermal conductivity value for a parylene/diamond composite material developed during this work. Chapter four will summarize this thesis and give some suggestions for further studies.

Chapter 2: Material Growth and Characterization

Molecular Beam Epitaxy (MBE)

Epitaxy means the growth of one or more thin crystalline layers on a substrate where the growth temperature is much lower than the melting point of the grown material or the substrate. The molecular beam epitaxy (MBE) technique has the ability to control precisely the thickness (to an atomic level), composition, and doping of these layers by changing the beam fluxes and substrate temperature. The ultra-high vacuum (UHV) pressure ($<1\times10^{-9}$ Torr) environment preserves the purity of the growing film and the surface of the growing film can be monitored *in situ* using a technique called Reflection High Energy Electron Diffraction (RHEED), Other *ex situ* characterization methods for MBE-grown layers include Hall effect, photoluminescence (PL), Auger electron spectroscopy, X-ray photoelectron spectroscopy (XPS), low-energy electron diffraction (LEED), secondary ion mass spectrometry (SIMS), and ellipsometry.[48,49]

IV-VI semiconductor materials have been fabricated by using many crystal growth techniques including liquid phase epitaxy (LPE) [50, 51], Bridgman-Stockbarger [52], spark plasma sintering [53], and chemical vapor deposition (CVD) [54]. The MBE technique for IV-VI semiconductor growth has been explored extensively by Dr. McCann's research group at the University of Oklahoma [44, 55, 56]. Figure 14 shows a schematic of an MBE system [57]. IV-VI semiconductor work in Dr. McCann's group has focused on developing methods for growth on industry standard silicon wafers where a modified Shiraki clean [55] is used before they are loaded into the MBE growth chamber. IV-VI (or lead salt) layers deposited on (100)-oriented Si substrates, with or without fluoride buffer layers, generally exhibit much inferior quality as compared to

the growth on (111)-oriented Si substrates. In addition, (100)-oriented layers with thicknesses over 0.5 μm tend to crack and peel off the Si substrate due to the thermal strains caused by the large differences in thermal expansion coefficients between the Si and the IV-VI layers, see Table 5 [58]. In contrast, (111)-oriented layers do not crack because of the efficient relaxation of the thermal strains by misfit dislocation formation and glide in (111) layers even at cryogenic temperatures. [59]

Table 5 Lattice constants, thermal expansion coefficient α at 300K, and energy band gaps of the IV-VI semiconductors and various substrates materials. ε_{th} (ΔT=300K) is the thermal strain.

Material	Lattice constant Å	α at 300K, 10^{-6} K^{-1}	ε_{th} (ΔT=300K) 100%	Band gap eV
PBSe	6.124	19.4	+0.012	0.278
Si	5.431	2.6	+0.52	1.17
CaF_2	5.463	19.1	+0.02	>5
BaF_2	6.2	18.8	+0.03	>5
CdTe	6.482	4.7	+0.45	1.49
GaSb	6.096	6.2	+0.41	0.75
InSb	6.478	5.4	+0.43	0.18

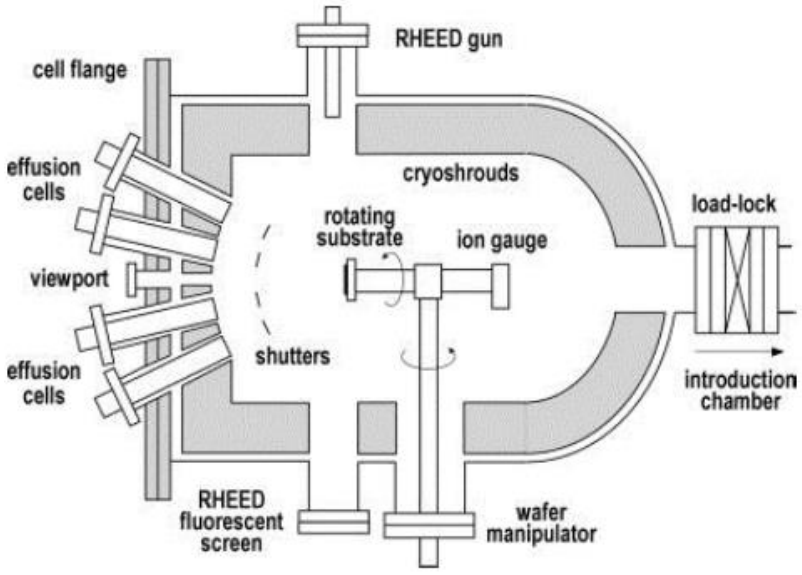

Figure 14 Schematic of an MBE growth chamber [57]

Despite the large lattice mismatch between Si and PbSe, high-quality IV-VI layers have been obtained on (111)-oriented Si substrates when using thin group II fluoride (CaF_2 and BaF_2) materials as buffer layers. [60] In this case, first a thin CaF_2 layer less than 100 Å thick and a subsequent BaF_2 layer of up to 3 μm thickness are deposited on the Si surface at temperatures up to 700℃. Later it was found that the BaF_2 can be omitted, and that the CaF_2 thickness should be below the critical thickness for strain relaxation (2nm at the growth temperature of 700℃. [58, 61]

Hall Effect Measurements

The Hall effect measurement is one of the most common electrical characterization techniques to measure electrical transport properties such as resistivity, carrier density, carrier type and the mobility of semiconductor structures. Figure 15 shows the Hall experimental set up. When a magnetic field is applied to a conductor perpendicular to the current flow direction, it produces a Lorentz force perpendicular to the magnetic field and the current. Carriers are deflected to an edge until steady state is reached when the Lorentz force on carriers is balanced by the force of the electric field due to carriers at the edges. This is known as the Hall Effect and the voltage drop perpendicular to the current direction is called the Hall voltage. [55]

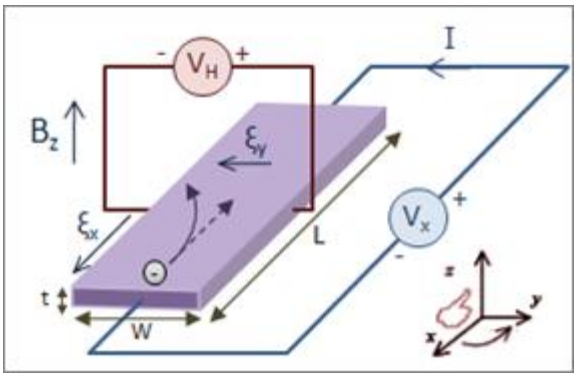

Figure 15 Hall Effect measurement setup for electrons [62]

When a current-carrying semiconductor is put in a magnetic field, the charge carriers of the semiconductor experience a force in a direction perpendicular to both the magnetic field and the current. The simple formula for the Hall coefficient given below becomes more complex in semiconductors where the carriers are generally both electrons and holes which may be present in different concentrations and have different mobility. [62] For moderate magnetic fields the Hall coefficient is

$$R_H = \frac{p\mu_h^2 - n\mu_e^2}{e(p\mu_h + n\mu_e)^2} \qquad (4)$$

Here n is the electron concentration, p is the hole concentration, μ_e is the electron mobility, μ_h is the hole mobility and e is the elementary charge. [63] $R_H = -1/(e \cdot n)$ is known as the Hall coefficient. The sign is opposite for holes. [49] The Hall measurement is performed on a square specimen, cleaved from the MBE grown wafer, using the van der Pauw, contact method [64], to determine the carrier density and the carrier mobility of the MBE grown materials. Once the steady-state conditions are reached, the Lorentz force is balanced by the Hall voltage and current continues to flow across the sample independent of the B field. The equation of motion for the electrons at the steady state is given by [65]:

$$-e\,(\mathbf{E} + \boldsymbol{v_d} \times \mathbf{B}) = \frac{m v_d}{\gamma} \tag{5}$$

This can be written in the tensor form:

$$\begin{bmatrix} E_x \\ E_y \end{bmatrix} = \begin{bmatrix} \frac{m}{e\gamma} & -B \\ B & \frac{m}{e\gamma} \end{bmatrix} \begin{bmatrix} v_x \\ v_y \end{bmatrix} \tag{6}$$

By Using $\boldsymbol{j} = -ne\boldsymbol{v_d}$ and $\mu = e\tau/m$, equation (6) can be rewritten in the form:

$$\begin{bmatrix} E_x \\ E_y \end{bmatrix} = \sigma^{-1} \begin{bmatrix} 1 & -\mu B \\ \mu B & 1 \end{bmatrix} \begin{bmatrix} j_x \\ j_y \end{bmatrix} \tag{7}$$

where $\sigma = en\mu$ is the zero B field conductivity.

The resistivity tensor can be written in the same form:

$$\begin{bmatrix} E_x \\ E_y \end{bmatrix} = \begin{bmatrix} \rho_{xx} & \rho_{xy} \\ \rho_{yx} & \rho_{yy} \end{bmatrix} \begin{bmatrix} j_x \\ j_y \end{bmatrix} \tag{8}$$

Where $\rho_{xx} = \frac{1}{\sigma} = \frac{1}{en\mu}$ (9)

And $\rho_{xy} = -\rho_{yx} = \frac{1}{en} B$ (10)

ρ_{xx} is called the longitudinal resistivity and ρ_{xy} is called the transverse resistivity or Hall resistivity and linearly increases with B in the low field limit.

At steady state, setting the transverse current j_y to zero in equation (8),

$$E_x = \rho_{xx} j_x \qquad\qquad E_y = \rho_{yx} j_x \tag{11}$$

From equation (10) and (11), transverse resistivity is given by:

$$\rho_{xy} = \frac{V_H}{I} = -\frac{1}{en_s} B \tag{12}$$

where V_H is the transverse voltage drop, I is the current passing through the sample and n_s is the sheet carrier density. It is related to the bulk concentration $n = n_s/t$, where t is the thickness of the epitaxial layer. The sheet carrier density is determined from the Hall coefficient, the slope of transverse resistivity versus B field. A linear Hall relationship is

observed for a single carrier type, and the carrier type (electrons or holes) is determined by the sign of $V_{H.}$

$$n_s = -\frac{1}{e}\frac{1}{(\frac{d\rho_{xy}}{dB})} \tag{13}$$

Mobility is calculated using the longitudinal resistivity at B=0 (equation 9) and the calculated carrier density as given in equation 13.

$$\mu = \frac{1}{en_s\rho_{xx}} \tag{14}$$

The Hall measurements were performed on a square specimen (1cm×1cm) as shown in Figure 16. In-Sn alloy was applied at the four corners of the sample for ohmic contacts. Temperature-dependent Hall effect measurements were done in a liquid nitrogen cryostat from 80K-350K.

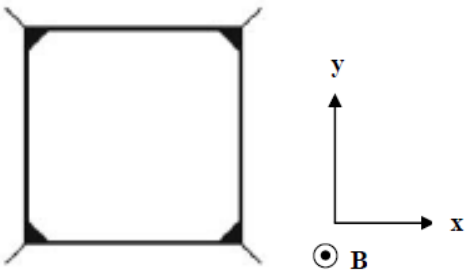

Figure 16 Geometry for van-der-Pauw Hall effect measurements

The IV-VI thin film samples were characterized by the ECOPIA Hall effect measurement system (HMS-5000) in magnetic fields up to 0.55 Teslas over the temperature range from 80K to 350K. Ohmic contacts were checked through observation of linear current voltage characteristics at room temperature. A linear Hall voltage with applied magnetic field was observed for all the samples at all temperatures. Figure 17 shows the ohmic contacts were applied on the measurements because of the observation on the linear current voltage characteristic at room temperature.

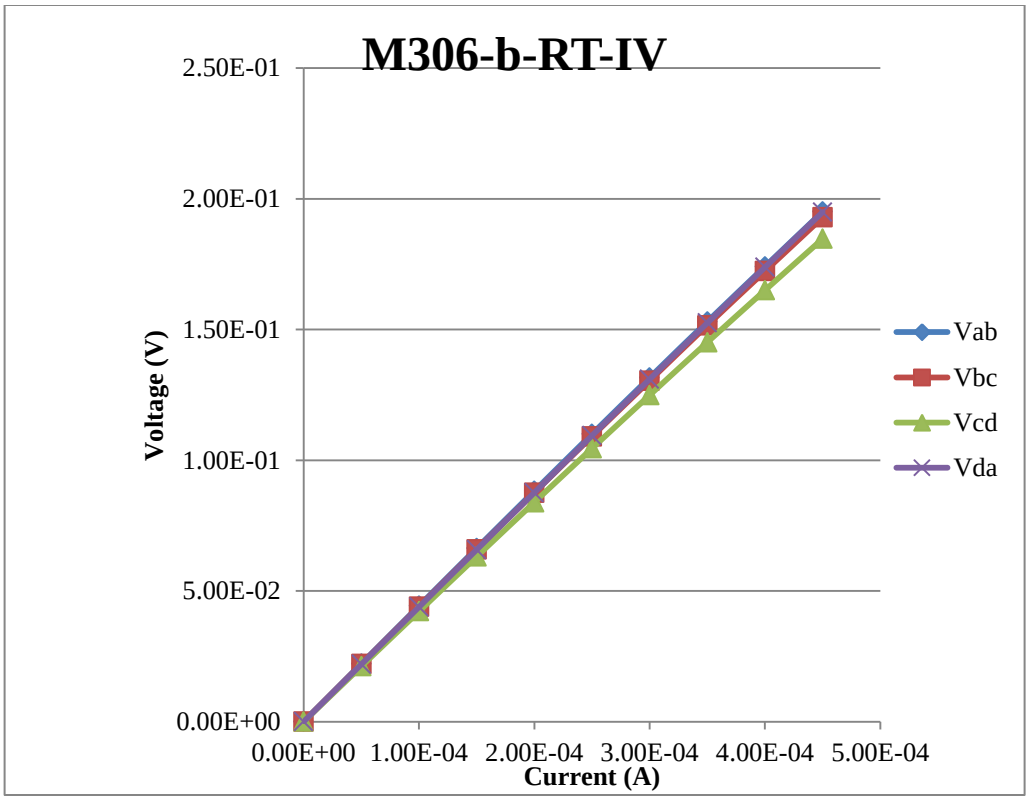

Figure 17 Ohmic contacts through observation of linear current voltage characteristics at room temperature.

Figure 18 shows the typical temperature dependence of the mobility and carrier density for a p-type PbSe/PbSrSe multiple quantum well (MQW) material on silicon with only CaF_2 as a buffer layer. The hole density decreases as the temperature decreases and saturates at low temperature. Furthermore, the hole mobility increases as the temperature decreases.

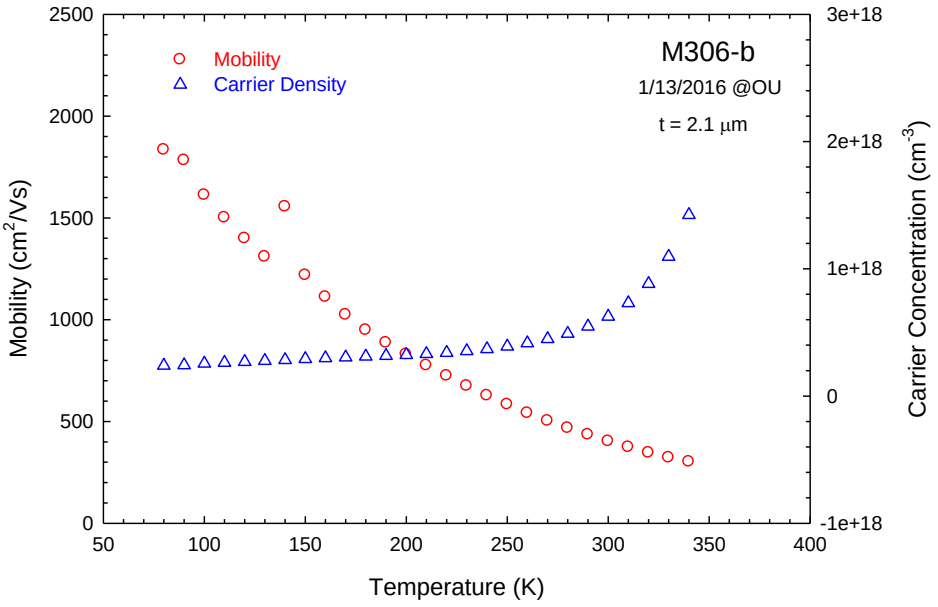

Figure 18 Hole density and mobility of PbSrSe MQW structure (M306-b) with only CaF_2 buffer layer as a function of temperature

The large dielectric constants lead to an effective screening of charged impurities. As a result, the scattering of free carriers by such impurities is rather weak in the IV-VI compounds, which results in high electron and hole mobilities at low temperatures, where mobility is higher due to less phonon scattering. In addition, due to the small band gap of IV-VI material, most donors and acceptors have defect energies within the conduction and valence bands, respectively, so complete carrier freeze-out is typically not observed even at very low temperatures. These properties make IV-VI materials rather insensitive to defects and impurities introduced during crystal growth or device fabrication processes and allow devices such as thermoelectric modules to operate well at low temperatures. [66]

Photoluminescence (PL) Spectroscopy

In a PL measurement the sample is optically excited by a pump beam, usually a laser light with photon energy greater than the band gap energy of the semiconductor sample, which generates electron-hole pairs that radiatively recombine to emit light. [67]

The PL measurement system used in this research was performed with a modular Fourier transform infrared (FTIR) spectrometer (Newport, Inc. Newport, RI model # MIR 8000) for broadband optical detection covering the energy range, 100meV $\leq E_{PL} \leq$ 400meV. The FTIR spectrometer was equipped with either a photoconductive HgCd Te or photovoltaic HgCdZnTe detector (Fermionics, Simi Valley, CA) with amplifier electronics and cutoff wavelengths of 10 μm and 6 μm, respectively. An optical power meter (Newport model # 1916-C) with a thermopile detector (Newport model # 818P-12) was used to measure the reflected and incident near-IR pump laser power. The sample mount stage temperature was stabilized with a thermoelectric (TE) cooler.

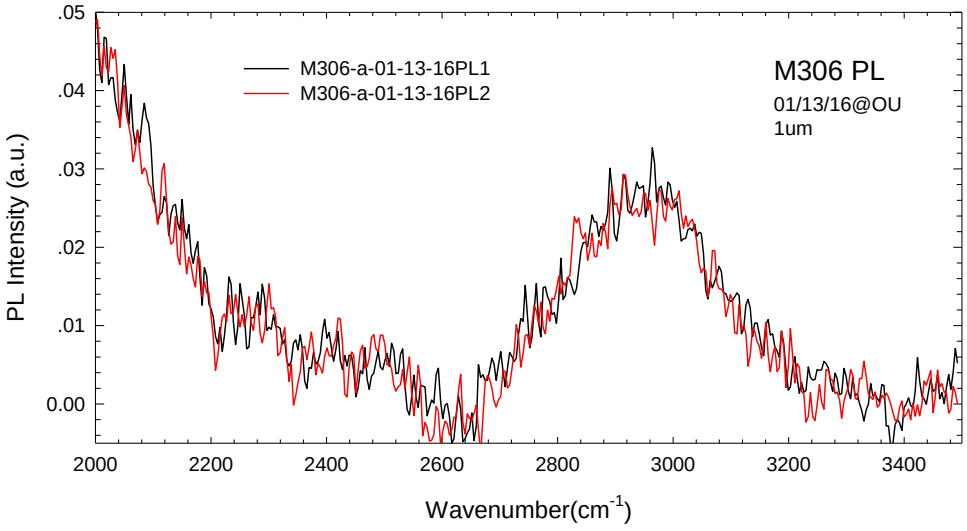

Figure 19 PL emission from sample #M306 from different laser spot positions

Figure 19 shows the PL emission from sample M306 for two different laser spot positions. The PL spectra match with each other well indicating that the IV-VI semiconductor MBE growth is uniform. Obtaining PL spectra as well as getting good Hall effect data from a PbSe/PbSrSe MQW layer with only CaF_2 as a buffer layer shows that this material has sufficient quality to be used as a temperature sensitive thin film material for an all optical (i.e. non-contact) temperature measurement method.

Reflection and Absorbance Measurements

The interaction of light with matter can be viewed macroscopically as being comprised of four components: an incident, a reflected, a transmitted, and an absorbed component. The reflectance can be defined in terms of the index of refraction of the media on either side of the interface. If the index of refraction of the material is n and the material is surrounded by air ($n_{air} \approx 1$), then the reflectance for near normal incidence can be written as, [68]

$$R = \left|\frac{n-1}{n+1}\right|^2 \tag{15}$$

The absorption coefficient is defined as the fraction of the intensity absorbed per unit length in the media, i.e.

$$\alpha = -\frac{1}{I(z)} \cdot \frac{dI}{dz} \tag{16}$$

This can be integrated to obtain Beer's Law

$$I(z) = I_{\circ} e^{-\alpha z} \tag{17}$$

Where $I_{\circ}$ is the intensity at the incident surface, i.e. z=o

$$\alpha z = -\ln\left(\frac{I}{I_{\circ}}\right) \tag{18}$$

The band structure of IV-VI materials result in particularly high values of the absorption constant and refractive indices in the mid-infrared region, factors that are important for their use in infrared detectors and emitters. The strong absorption of photons with energies above the fundamental energy gap is due to the particularly high joint density of states at the direct energy gap at the L-points of the Brillouin zone arising from the eightfold valley degeneracy (including electron spin). This is one of the main advantages of the IV-VI compounds compared to narrow-gap III-V or II-VI semiconductors such as InSb or HgCdTe, which have direct gaps at the Γ-point of the Brillouin zone. While the transverse effective masses of the carriers in IV-VI compounds are comparable to those of the narrow-gap III-V and II-VI compounds, their longitudinal effective masses are much larger, which together with the eightfold valley degeneracy leads to a substantially higher joint density of states for electronic transitions between the valence and conduction bands and thus, to much more efficient photon absorption. [66]

Figure 20 is the absorption (using reflection geometry) measurement systems at the University of Oklahoma. Flat mirror PYREX whose reflectance is more than 96% is used as the reference during the measurement.

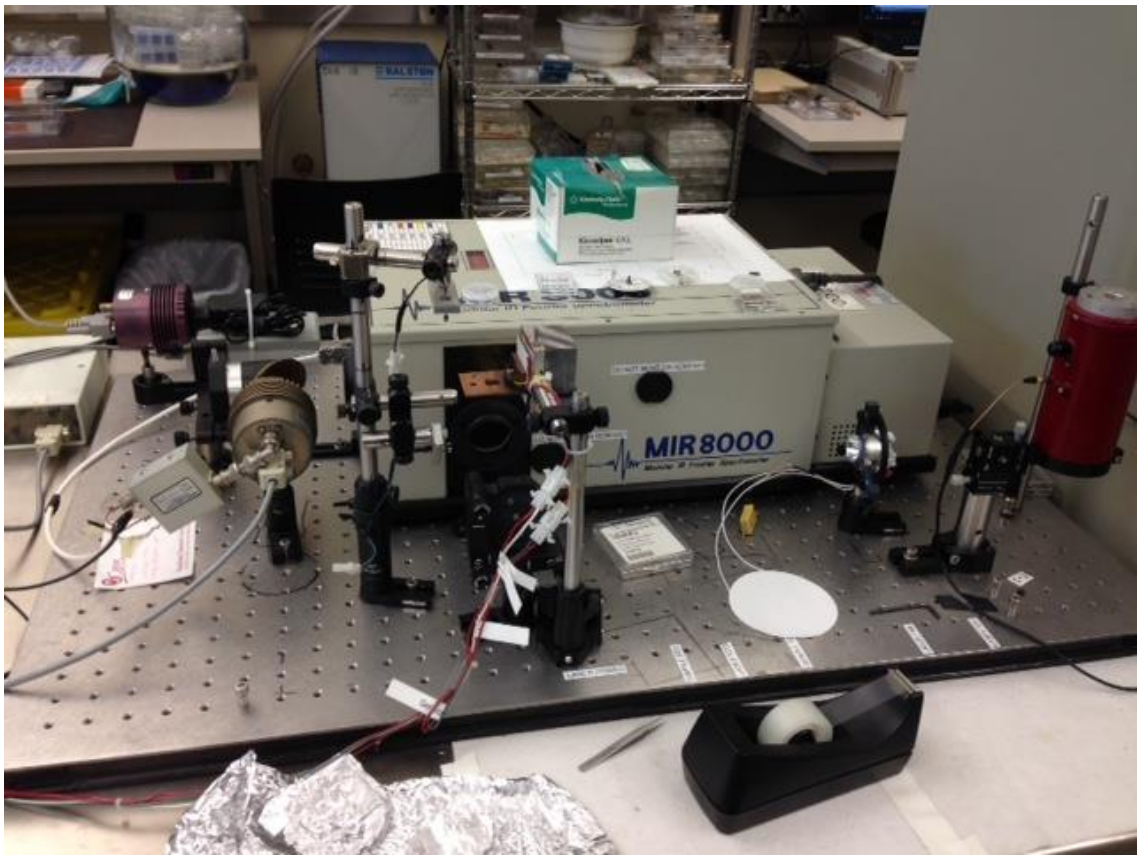

Figure 20 Absorption (using reflection geometry) measurement systems at the University of Oklahoma

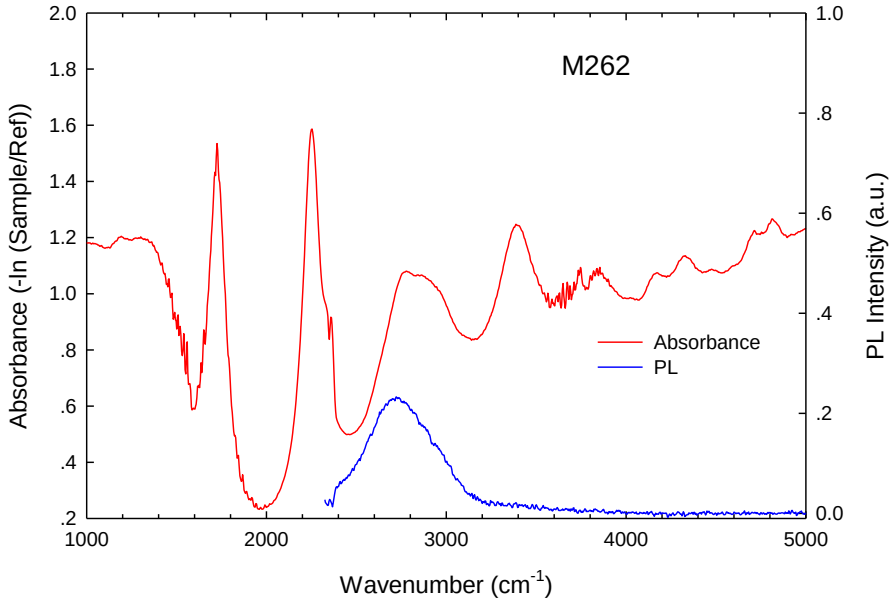

Figure 21 Experimental photoluminescence and the absorption (using reflection geometry) of a MBE grown PbSrSe MQW pn junctions (#M262) at room temperature are shown.

Figure 21 shows photoluminescence and the absorption data (using reflection geometry) of a MBE grown PbSrSe MQW pn junctions (#M262) at room. The increase in optical absorption takes place whenever the photo energy exceeds the energy separation between the confined quantum well electronic states. Super-imposed on this are Fabry-Perot interference fringes due to multiple reflections of the optical waves at the IV-VI epilayer surface and the IV-VI-CaF2 interface. [69]

Chapter 3: Diamond and Parylene Composite Bonding

Parylene-C Bonding

Parylene, unlike conventional polymers, does not go through a liquid-to-solid phase transition; instead it can be directly vapor-deposited from a solid powder to a solid film. Therefore, parylene does not create a strong covalent bond because it does not go through a curing process; it is deposited as a thin film through vapor deposition. Second, parylene becomes an inert film when deposited. Parylene is a high molecular weight and crystalline polymer, and it consists of carbon backbones without any oxygen, nitrogen, or sulfur atom links. This crystalline carbon backbone film is naturally stable and highly resistant to chemical attacks. Parylene can also be used as a bonding material. [70]

The most common parylene is parylene C followed by parylene D and parylene N. The melting point of parylene C is lower than that of parylene D and parylene N. Parylene C can have a high deposition rate while still possessing a high degree of uniformity. [71] Figure 23 shows the atomic structure of parylene C molecular chains. Table 6 shows the main physical properties of parylene C.

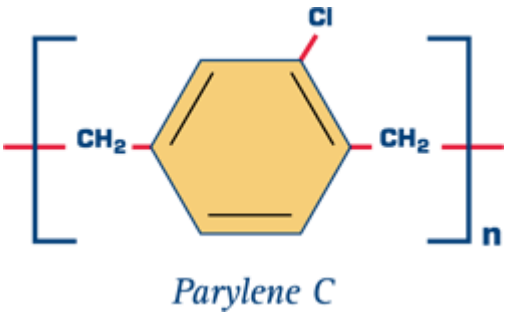

Figure 22 schematic of parylene C molecule chains

Table 6 The main physical properties of parylene C

Electrical conductivity	**$10^{-14}\Omega.\,m$**
Melting point	**290 ℃**
Thermal Conductivity	**0.084 W/mK**
Specific Heat (C)	**0.712J/(g*K)**

Parylene C thin films were deposited after Si (100) chips (1cm x 1cm) were cleaned by squirting with acetone and methanol and O_2 plasma exposure for 30 seconds under 100W power and 200mTorr O_2 pressure. Immediately before bonding, the parylene-coated chips were exposed to an O_2 plasma for 10 seconds at the same 100 W power and 200mTorr O_2 pressure. Figure 23 is a photograph of the vacuum bonding system used for this work. The chips were loaded parallel into the bonding chamber as depicted in the Figure 24. The chamber was pumped down to 10^{-3} Torr with a mechanical vacuum pump, and the chips were heated to 290℃ while a translation stage was used to maintain an applied force of about 1kg/cm^2 or about 100KPa), corresponding to a load cell reading of 8. Figure 25 gives the vacuum bonding system force load calibration.

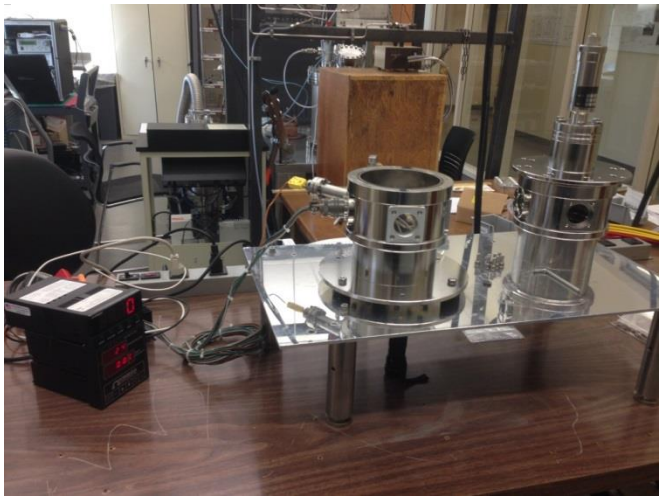

Figure 23 Schematic of parylene C vacuum bonding system

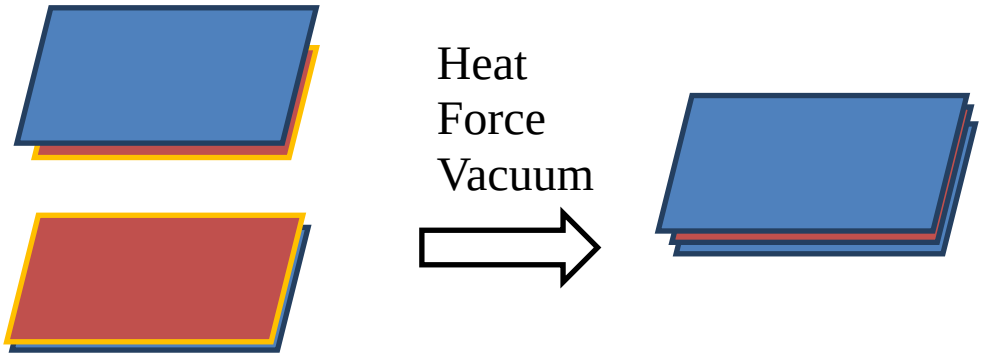

Figure 24 The sandwich structure of Si chips parylene C bonding

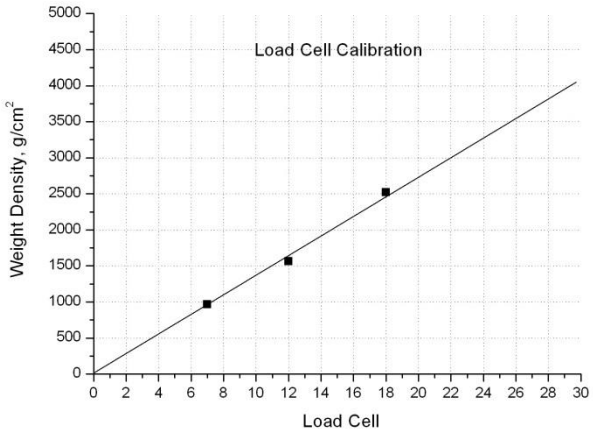

Figure 25 parylene C vacuum bonding system force load calibration

Bonded Si (100) chips were cleaved to get the cross section image to assess bonding quality. Figure 26 and Figure 27 are optical microscope cross section images of parylene C bonded Si (100) chips. SEM images, Figure 28 and Figure 29, show that the parylene C bonding is uniform with no voids and a thickness of less than 1 μm.

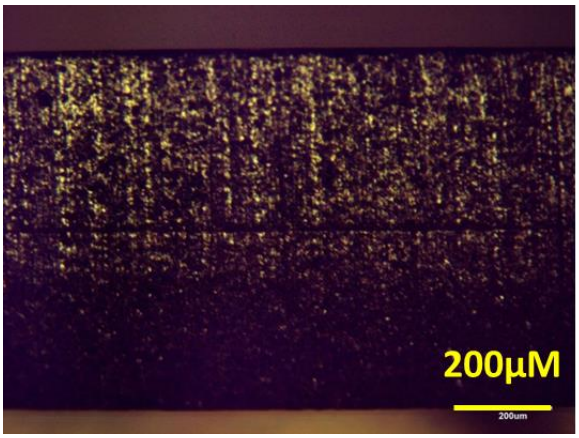

Figure 26 Optical microscope cross section image after parylene C bonding Si (100) chips in larger scale

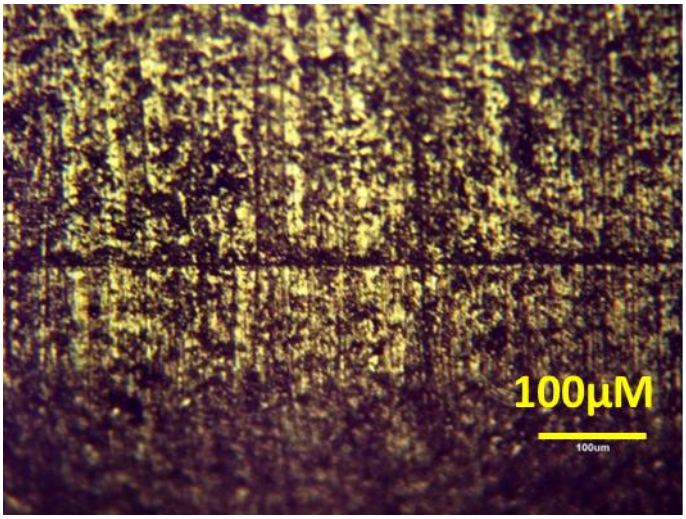

Figure 27 Optical microscope cross section image after parylene C bonding Si (100) chips in large scale

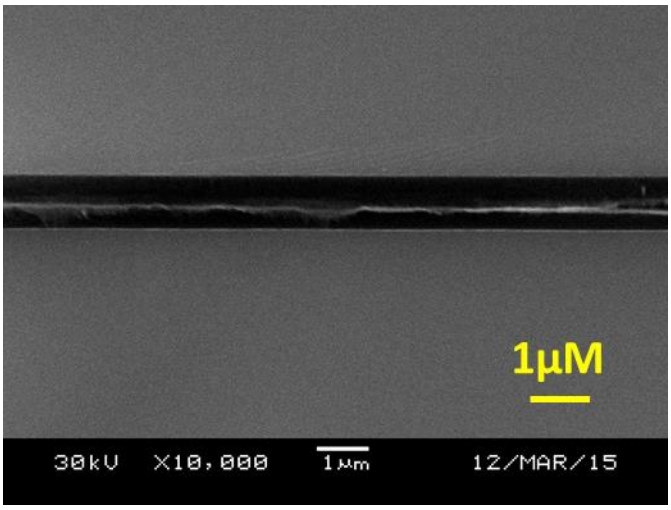

Figure 28 SEM cross section image on parylene C bonding Si (100) chips in small scale

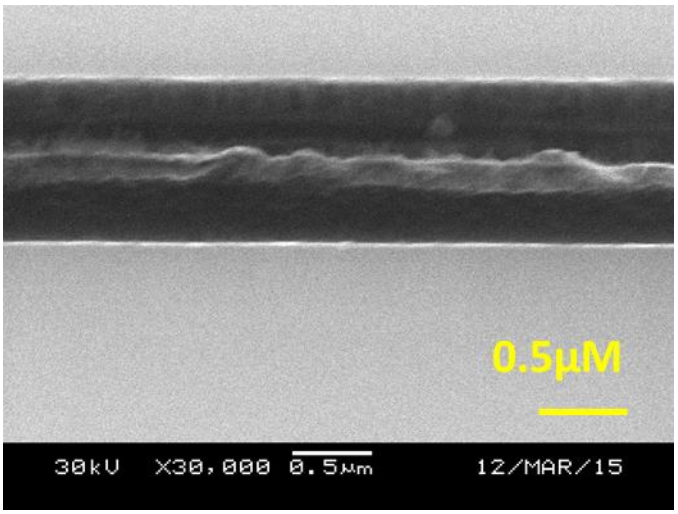

Figure 29 SEM cross section image after parylene C bonding Si (100) chips in smaller scale

Parylene-C and Diamond Composition Bonding

The main requirements placed by electronics engineers on heat sinks, formulated possibly not in the order of descending significance, are: [11]

(1) High thermal conductivity.

(2) Low cost

(3) Low electrical conductivity

(4) Thermal expansion coefficient of the heat sink should be equal to that of the material to be cooled

(5) Low loss tangent

(6) Small weight

A bonding material composed of a diamond/parylene composition is a new option with many potential benefits. For example, thermal expansion coefficient of a composite material can be adjusted. Table 7 lists the thermal conductivity and thermal expansion coefficients at room temperature of semiconductor device materials and packaging

materials most widely employed in heat sink fabrication. Lots of research has been done on the diamond and copper composite material. Figure 30 shows the enhancement of thermal conductivity when the diamond volume fraction is increased. The thermal conductivity in the diamond-copper system is calculated in the frame of the Maxwell model, and the thermal expansion coefficient in terms of the models of Turner and Kerner. The grey circle indicates experimental values of the thermal conductivity and thermal expansion coefficient

Table 7 Thermal conductivity and thermal expansion coefficients at room temperature of materials most widely employed in heat sink fabrication

Material	Thermal conductivity, λ W/(m·K)	Thermal expansion coefficient, $\alpha \cdot 10^6$, K^{-1}
Synthetic Diamond (C)	1,000-2,200	1.1
Silicon (Si)	153	3.8
Silicon Carbide (SiC)	280-400	3.8
Aluminum Nitride (AlN)	285	4.3
Indium Phosphide (InP)	68	4.3
Gallium Arsenide (GaAs)	55	5.9
Copper (Cu)	380	16.5
Silver (Ag)	420	19.8
Aluminum (Al)	240	22

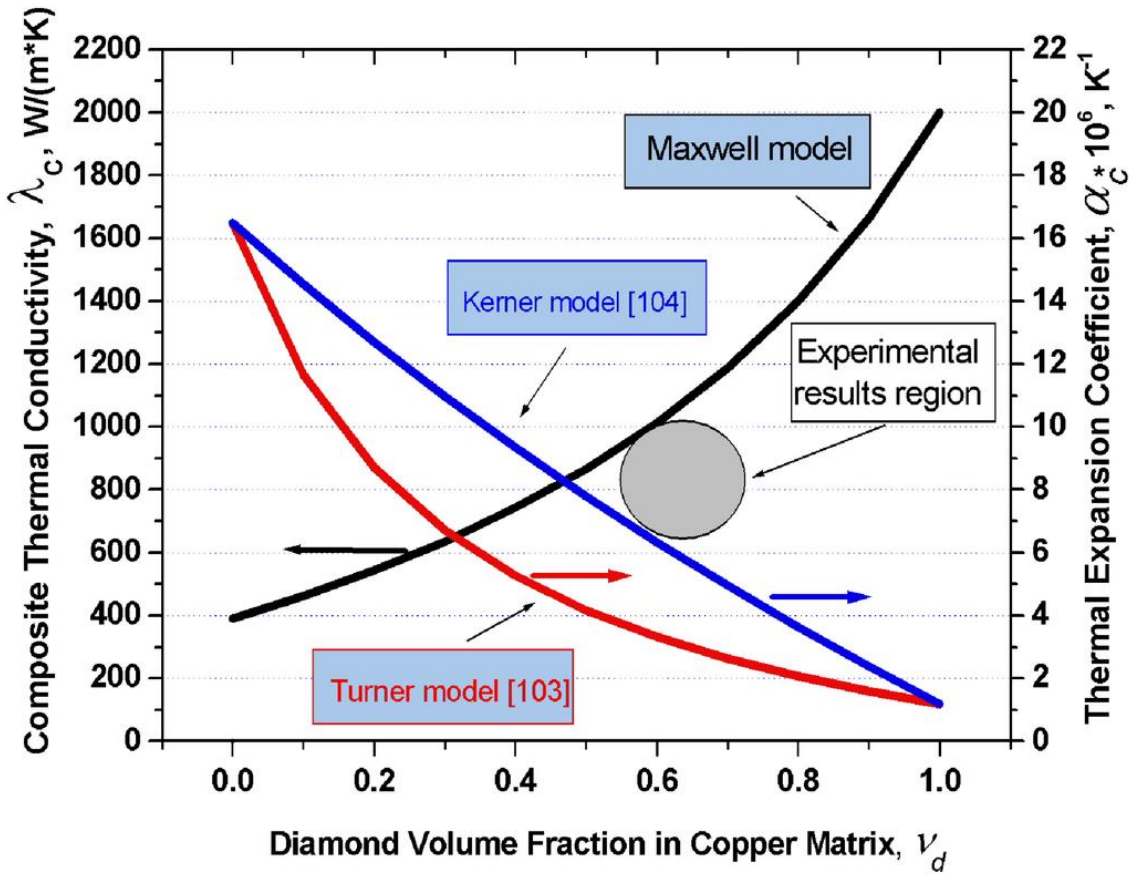

Figure 30 Thermal conductivity in the diamond-copper system [11]

Figure 31 outlines the experimental steps involved in forming a diamond/parylene composite bonding material. After a general clean (DI water, methanol and acetone) and O_2 plasma exposure for 10 seconds, ~1 μm thickness of parylene C was deposited on the Si (100) chips. A uniform diamond particle layer was then deposited on top of each parylene-coated chip. A second parylene C layer was then deposited after a 10 second O_2 plasma exposure under 100 W power and 200 mTorr O_2 pressure to encapsulate the diamond particle layer. The chips were then after cleaned by DI water, methanol and acetone and O_2 plasma exposed for 10 seconds and loaded into the bonding chamber and bonded using the same conditions as described above.

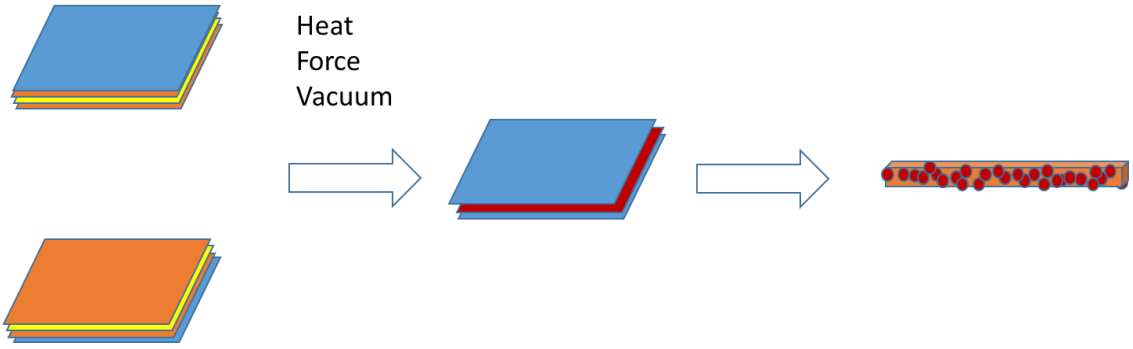

Figure 31 The process on Diamond-parylene composite Bonding

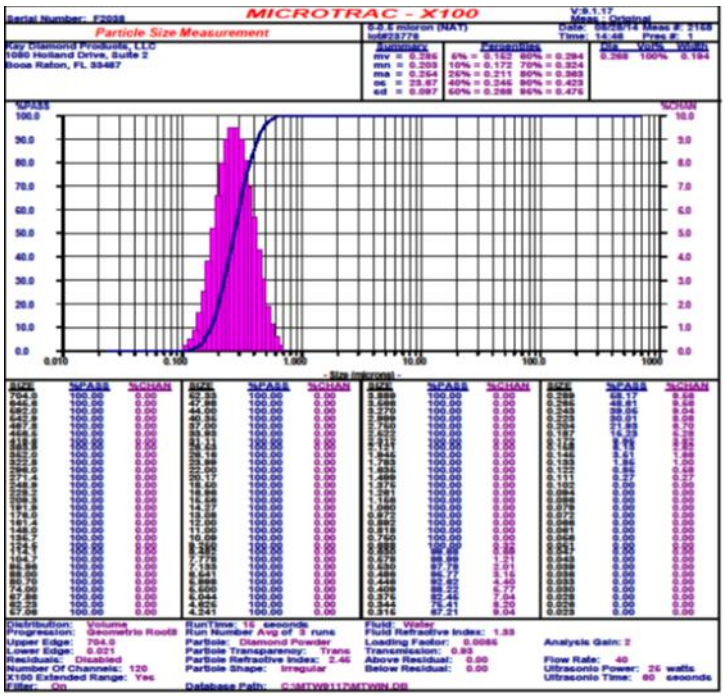

Figure 32 Small Diamond Particle Size Histograms

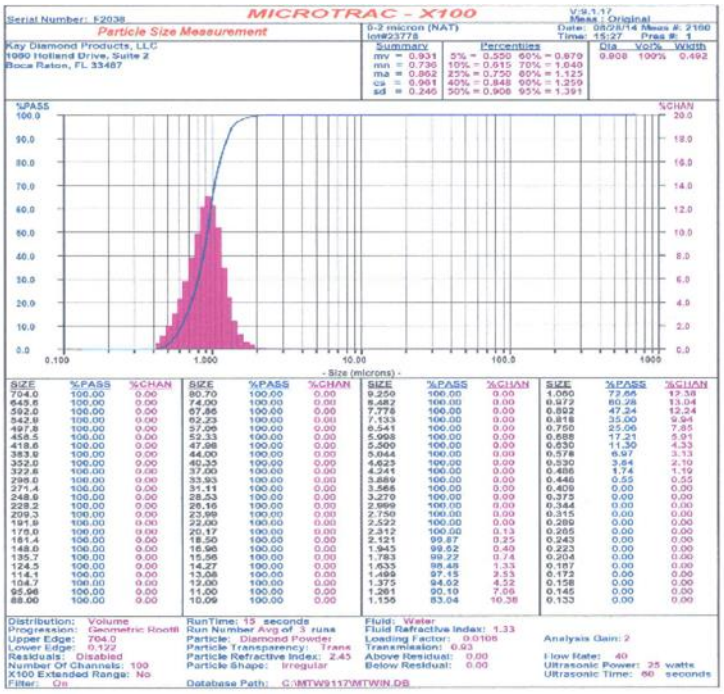

0-2μm

Figure 33 Large Diamond Particle Size Histograms

Figure 32 and Figure 33 are the data on the diamond particles. Natural diamond particles from Kay Diamond Products (KDP), Boca Raton, FL were used. The small diamond particles (0~0.5μm) were put into distilled water to make a suspended solution. This solution was mixed in an ultrasonic cleaner for around 15 minutes before the deposition. The liquid was deposited using a needle tube see Figure 34. Figure 35 is an SEM image showing diamond particle coverage of a parylene-coated chip. Red circles represent a lack of coverage. At first, a quick dry process was used. After the liquid solution deposition, the chips were heated to 100℃ for about 1 minute. Figure 36 shows

a parylene/diamond-coated Si (100) chip with a low concentration (0.035/50ml) after a quick dry process.

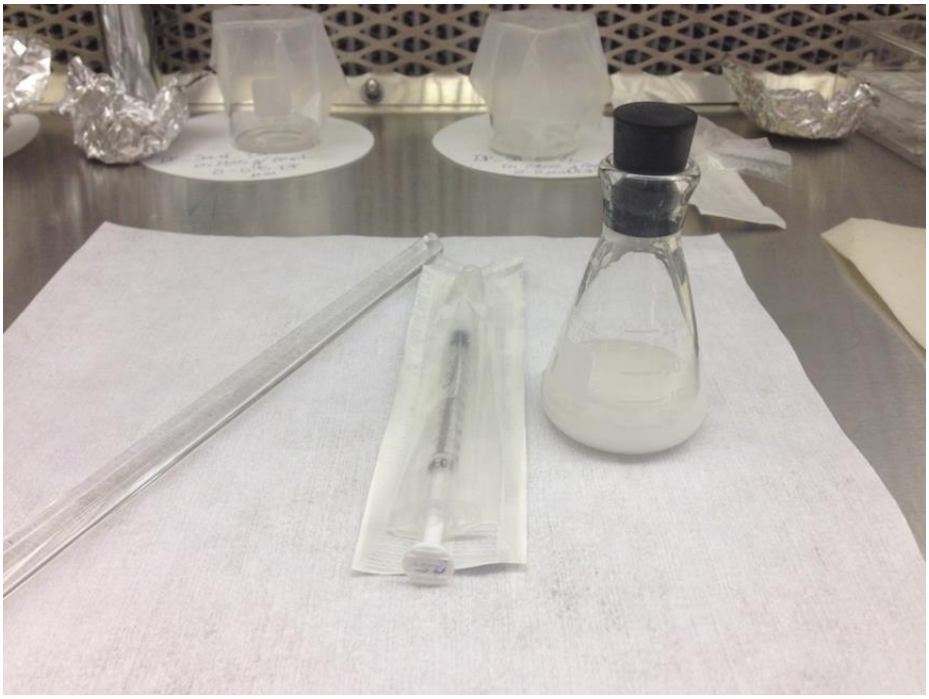

Figure 34 Diamond and distill water solution

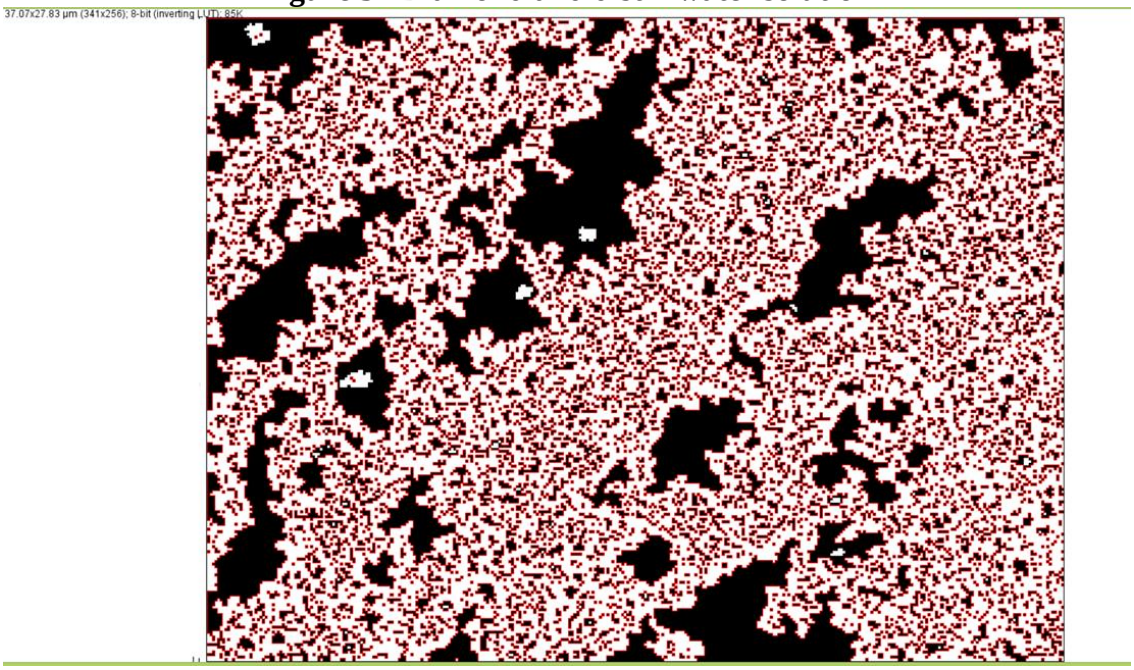

Figure 35 Diamond Particles coverage analysis with 0.035g/50ml

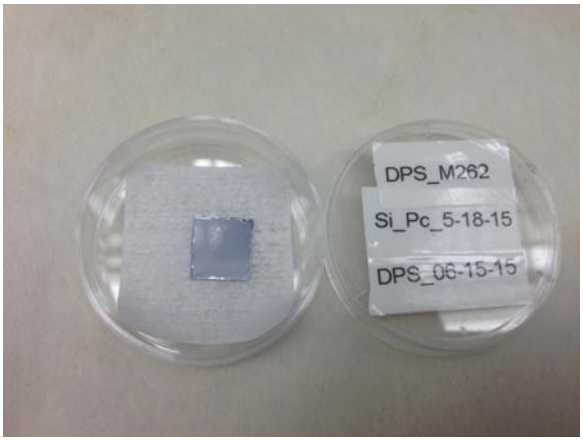

Figure 36 The quick dry process parylene-diamond deposition chip with low concentration

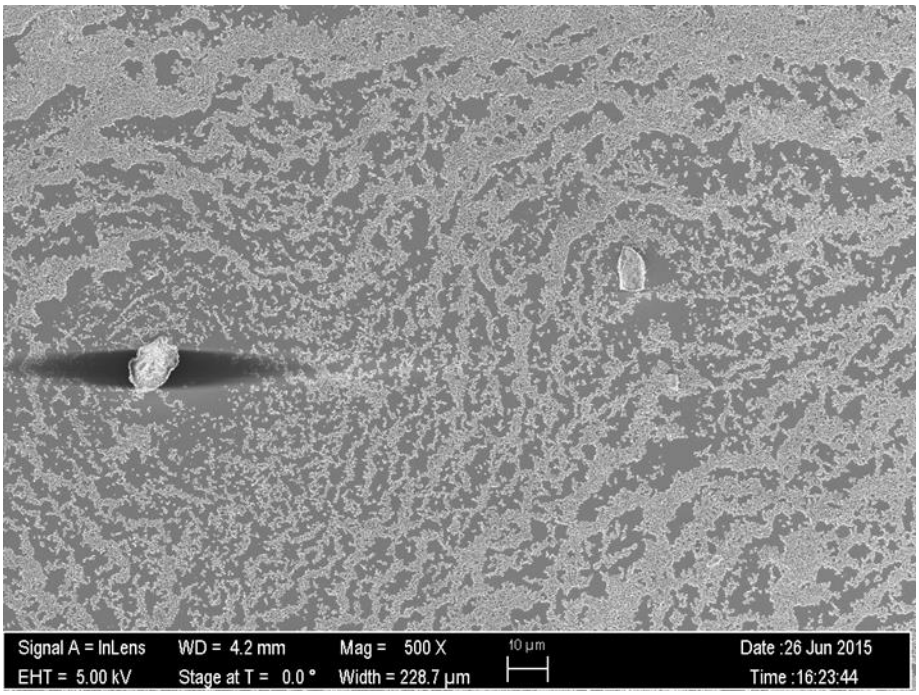

Figure 37 SEM image of diamond deposition on a parylene-coated chip after quick drying without wafer cleaning process.

SEM images, see Figure 37, showed some dust contamination on the chip. Therefore, before the any deposition steps, a deep clean of the chip should be done. The Si (100) wafers after being cleaved into chips were loaded into the ultrasonic cleaner with DI

water for 3 minutes, methanol for 3 minutes and acetone for 3 minutes. After this deep clean procedure and the parylene-diamond deposition procedure described above, the dust particles disappeared, see Figure 38.

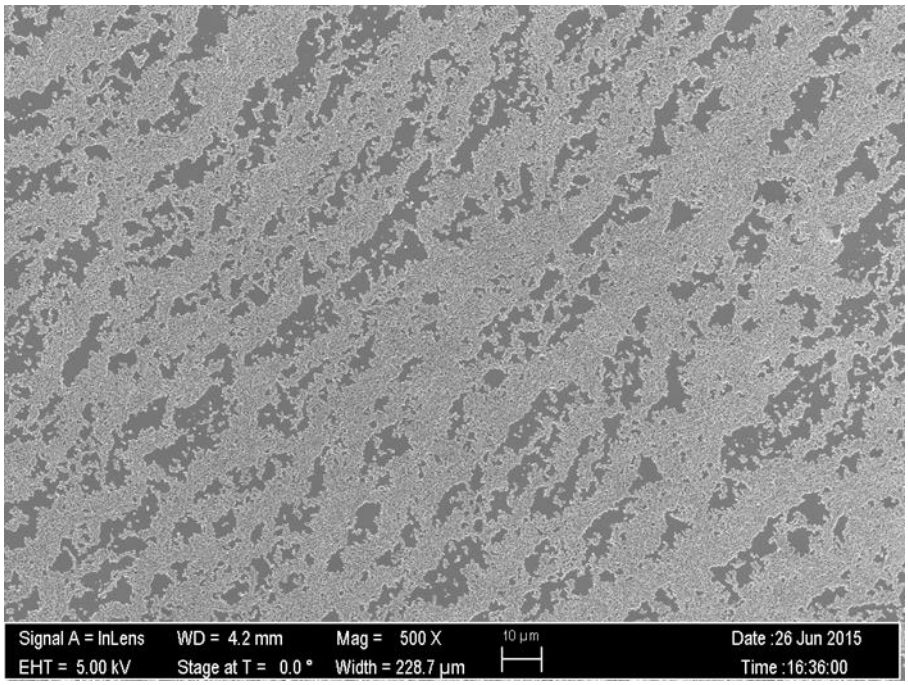

Figure 38 SEM image of the quick diamond deposition on a parylene-coated chip after quick drying with wafer deep cleaning process

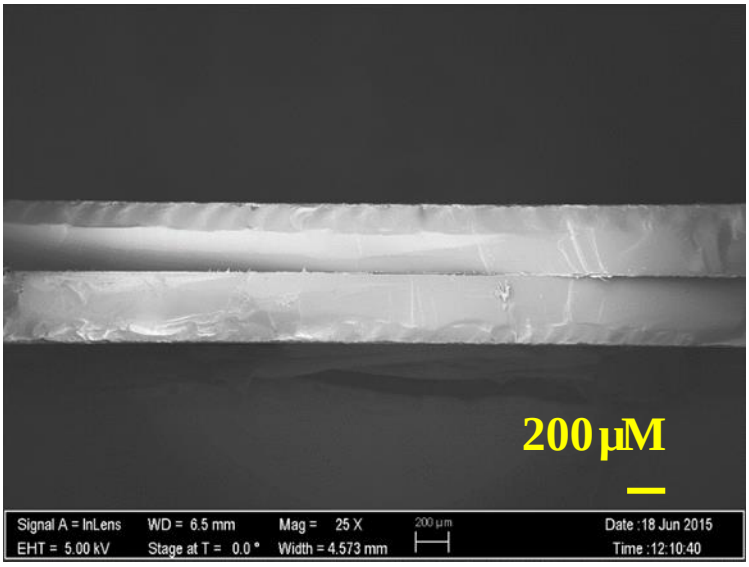

Figure 39 SEM cross section image of the low solution parylene and diamond composite Si (100) bonding sample in larger scale

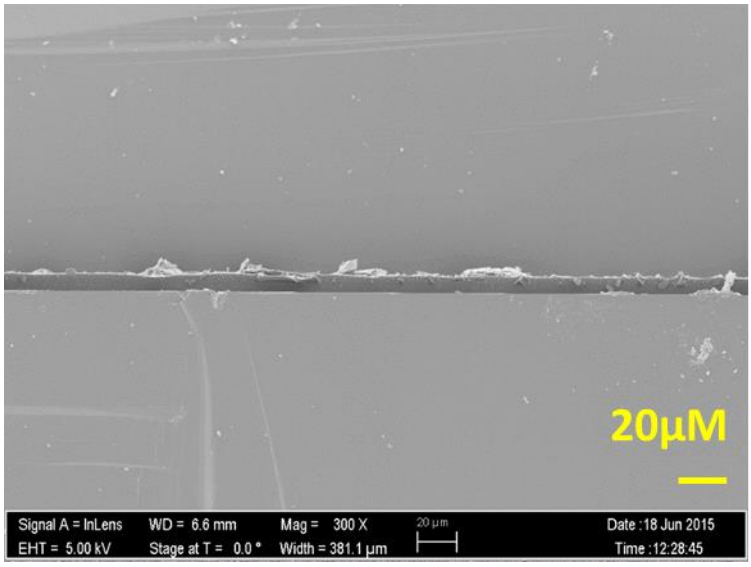

Figure 40 SEM cross section image of the low solution parylene and diamond composite Si (100) bonding sample in larger scale

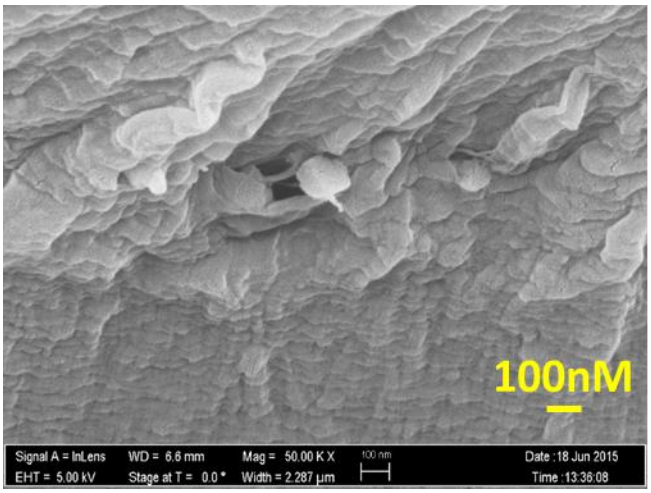

Figure 41 SEM cross section image of the low solution parylene-diamond composite Si (100) bonding sample in small scale

Figures 39-42 show SEM cross sectional images of bonded Si (100) chips made with a low concentration diamond particle solution (0.035g/50ml). The diamond particles can be seen in the highest magnification images (Figure 42). The small diamond particles were used in these samples.

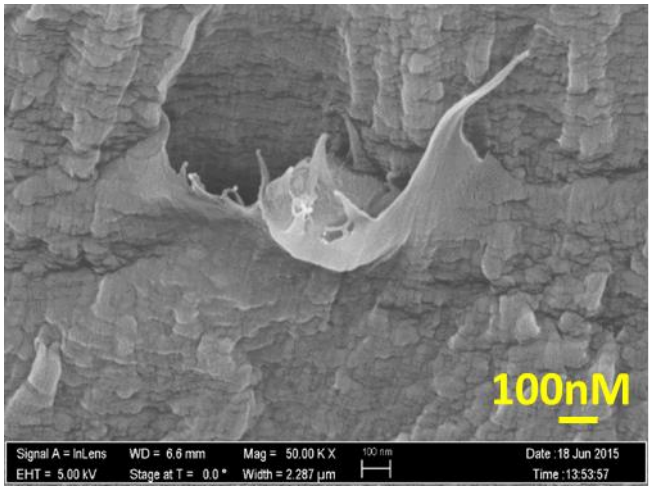

Figure 42 SEM cross section image of the low solution parylene and diamond composite Si (100) bonding sample in smaller scale. Diamond particle can be seen is this image.

The next step is to bond a IV-VI semiconductor epitaxial layer to the parylene-diamond coated Si (100) chip. For a control sample, a IV-VI layer was also bonded to a parylene-only coated Si (100) chips. IV-VI layers from MBE sample number M262, which had good PL emission intensity, were used as outlined in Figure 44 and Figure 45. The chips were cleaned by DI water, methanol, acetone and O_2 plasma exposure for 10 seconds. They were then bonded using the same conditions described above.

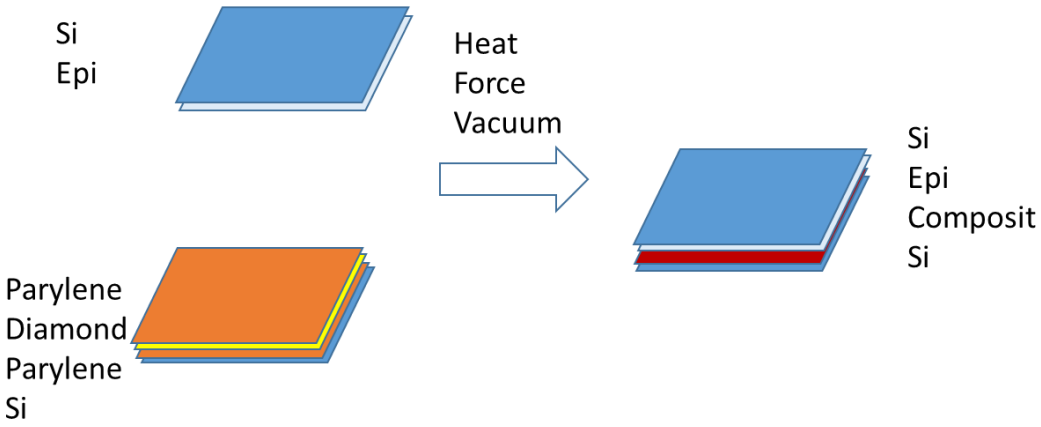

Figure 43 Si (111) chip with epi layer was bonded to parylene-diamond chip

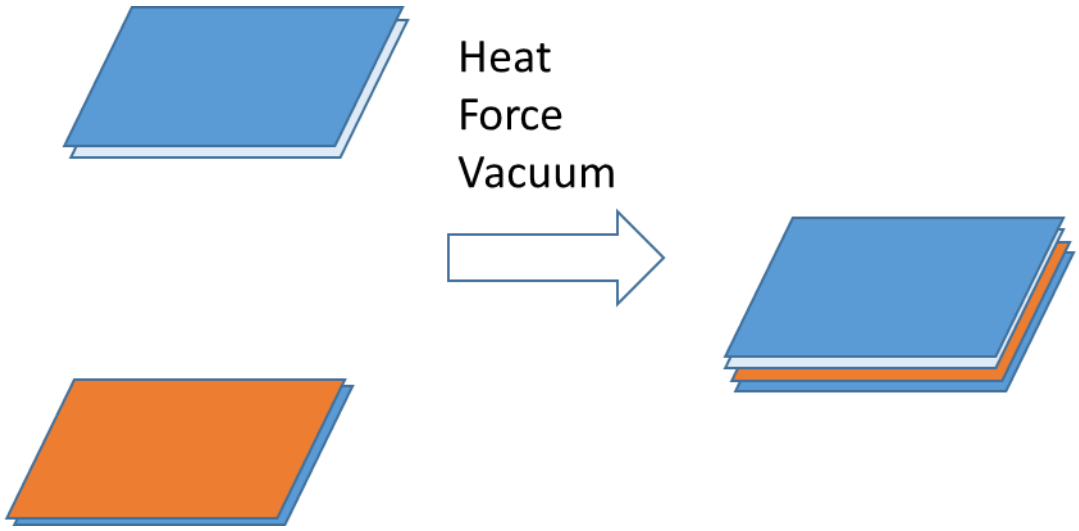

Figure 44 Si (111) chip with epi layer was bonded to parylene-only chip

Primary Results on Flip-chip bonding

After the bonding, one side of the sample is Si (111) and the other side is Si (100). The PL comes from an epi layer grown on the Si (111) side. Figure 45 shows PL spectra from MBE sample number M262 bonded with a parylene-diamond composite material. The red curve is the PL spectrum obtained through the Si (100) chip, which is lightly-doped p-type, and the black curve is the PL spectrum obtained from Si (111) chip, which is heavily-doped p-type. These data clearly show that the Si (100) chip is transparent to both the ~1μm wavelength laser and the 4μm PL wavelength. Figure 46 shows the PL emission spectra from M262 boned with only parylene to a lightly-doped p-type Si (100) chip.

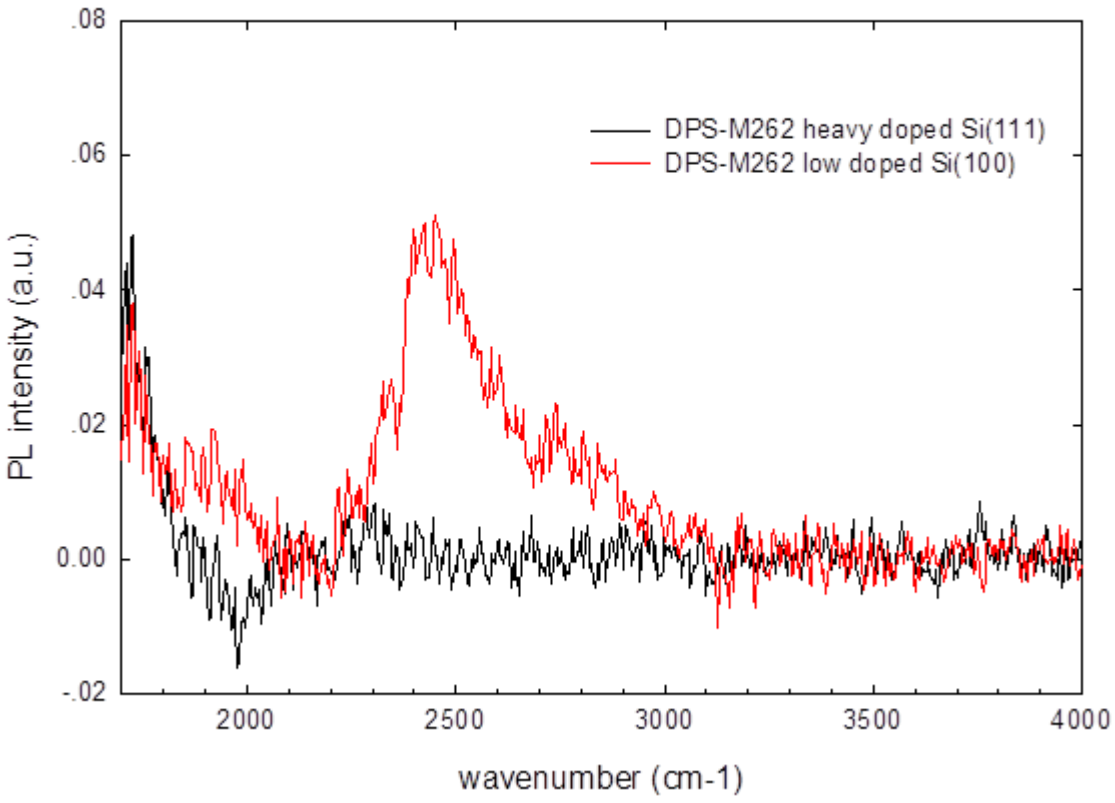

Figure 45 PL data on M262 unlifted-off parylene-diamond composite bonding sample at the room temperature

Figure 48 is relationship on the n/p type silicon wafer resistivity and dopant concentration. Heavily doped Si wafer has low resistivity, and low doped Si wafer has high resistivity. After we know the doping level and type, the Si optical absorption corresponding to light wavelength the optical absorption coefficient can be estimated according to figure 49.

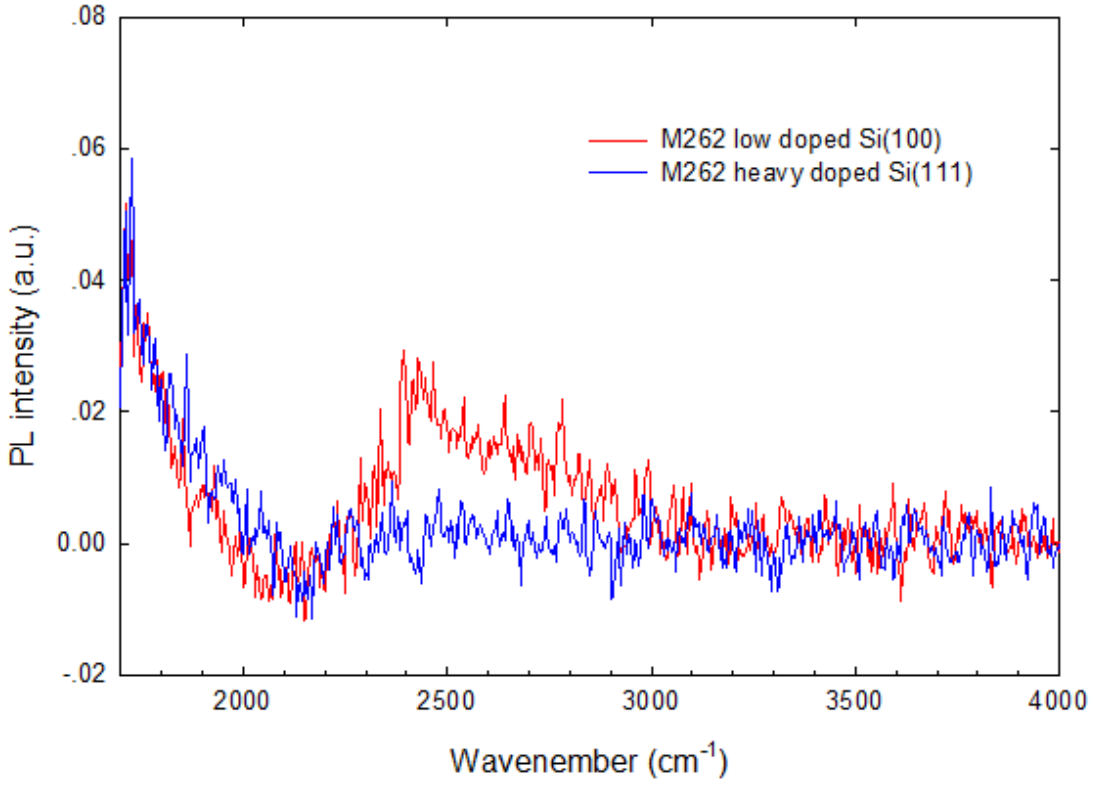

Figure 46 PL data on M262 unlifted-off parylene-only bonding sample at the room temperature

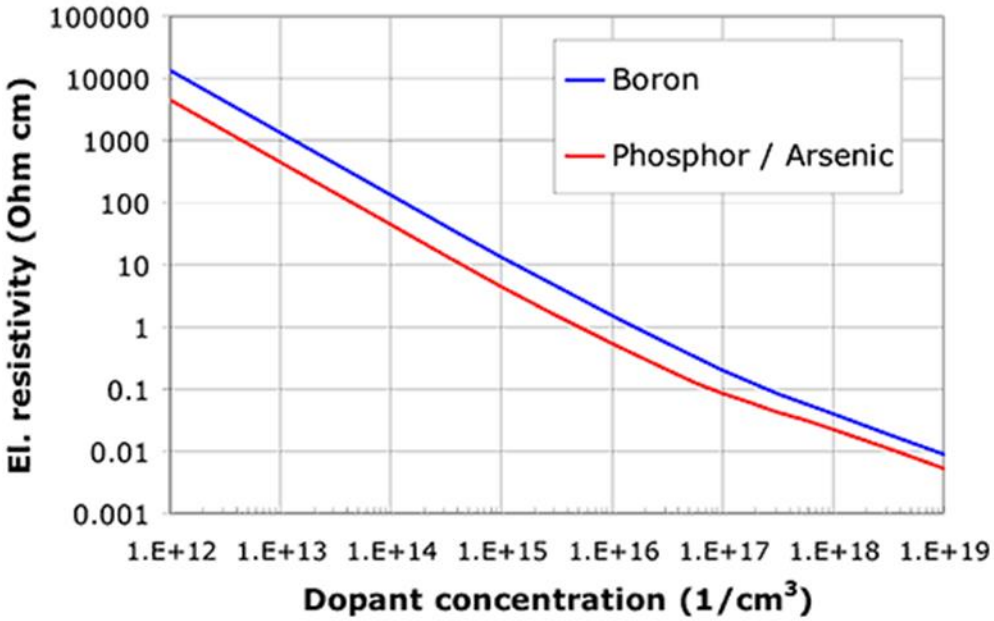

Figure 47 Si wafer doping and resistivity [74]

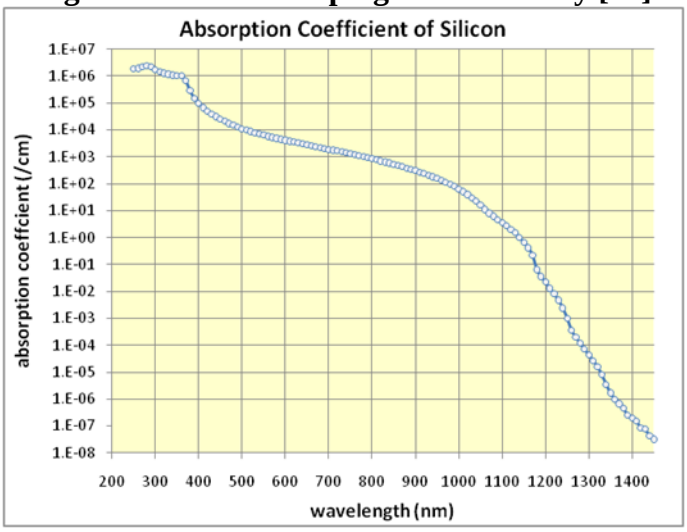

Figure 48 Si optical absorption and light wavelength [75]

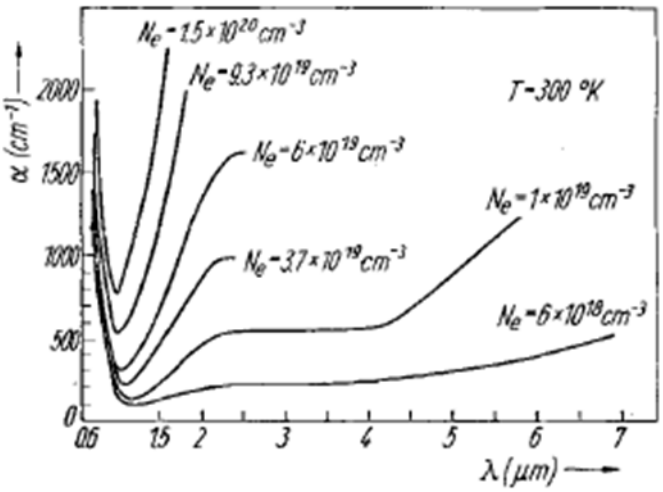

Figure 49 Si wafer doping level and optical absorption [76]

From figure 49 the heavily doped Si wafer has a larger optical absorption coefficient, the low doped Si wafer has smaller optical absorption coefficient.

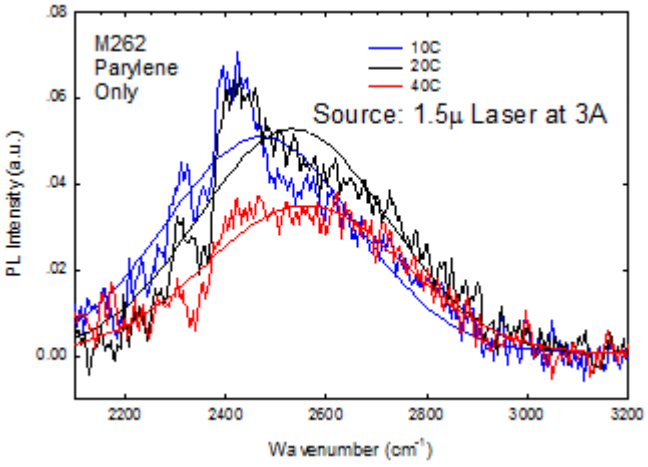

Figure 50: PL emission spectra from M262 before growth substrate removal on a parylene-only bonded sample for different TEC stage temperatures at the same laser power density

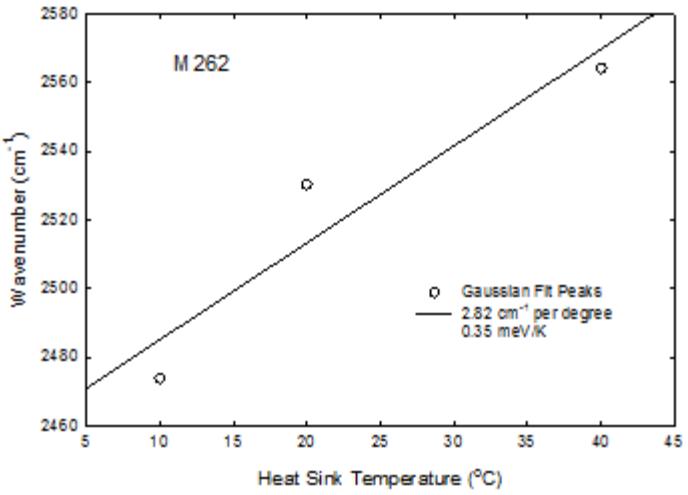

Figure 51: PL Peak energy from M262, before growth substrate removal on a parylene-only bonded sample for different TEC stage temperatures at the same laser power density

Figure 50 shows PL emission spectra data from M262, before growth substrate removal, on a parylene-only bonding sample for different TEC stage temperatures and the same laser power density. The PL emission peaks were fitted with Gaussian functions, and these peaks were plotted as a function of the TEC stabilized heat sink temperature, see Figure 51.

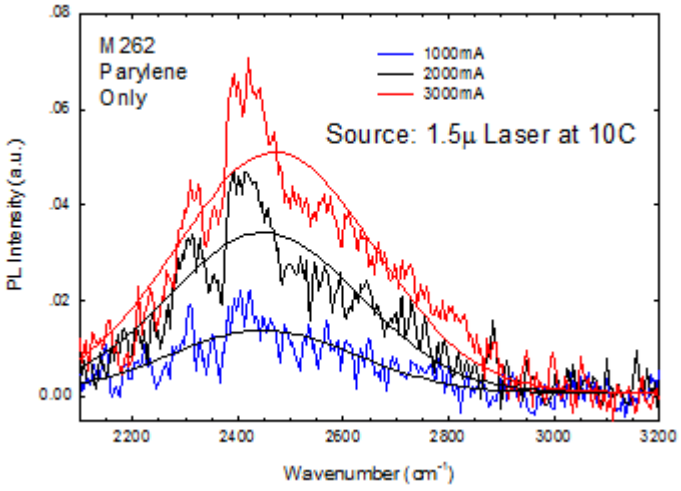

Figure 52: PL emission spectra from M262, without growth substrate removal, on a parylene-only bonded sample for different laser power densities at the same TEC stage temperature

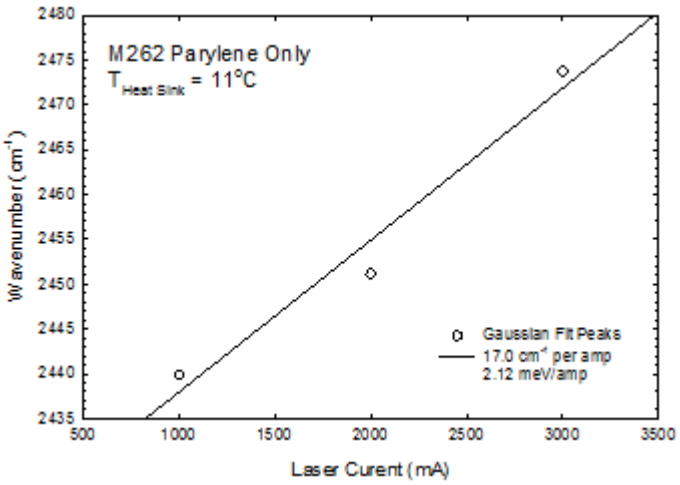

Figure 53: PL Peak energy from M262, without growth substrate removal, on a parylene-only bonded sample for different laser power densities was set at the same TEC stage temperature

Figure 52 is PL emission data from M262, before growth substrate removal, on a parylene-only bonding sample with different laser power densities at the same TEC stage temperature. The blue shift on the PL peak indicates localized heating when the laser power density is increased. The Gaussian fitted emission peak wavelength versus laser current is shown in Figure 53. It is about 6℃ (17 cm^{-1}/A/2.82 cm^{-1}/℃) of heating per amp from 1A to 3A for the parylene-only bonded substrates.

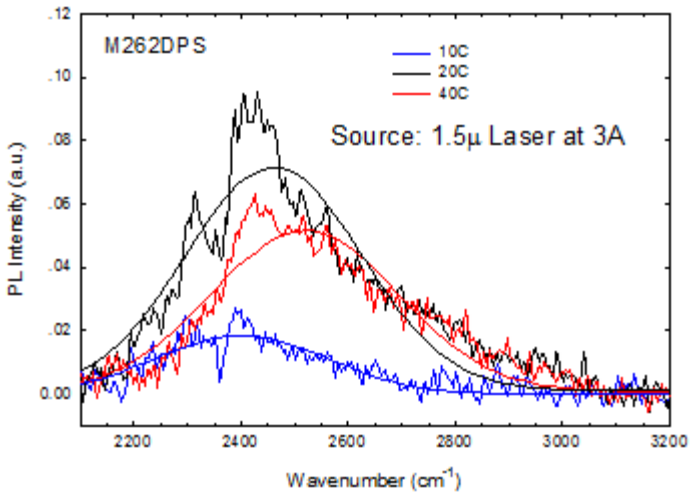

Figure 54: PL emission spectra from M262, without growth substrate removal, on a parylene-diamond composite bonded sample for different TEC stage temperatures at the same laser power density

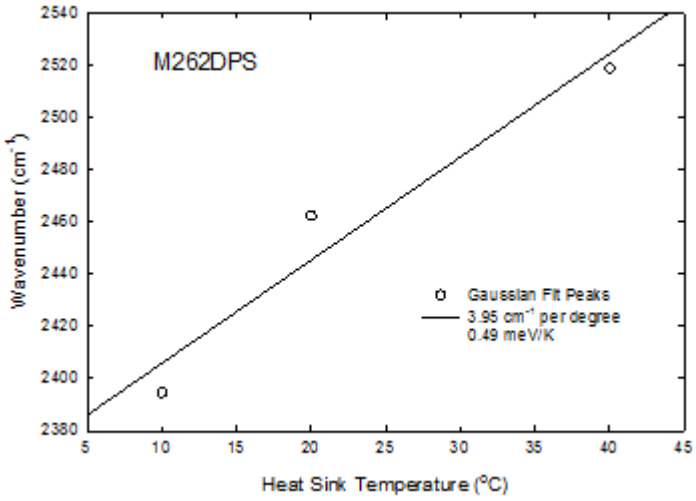

Figure 55: PL Peak wavenumbers from M262, without growth substrate removal, on a parylene-diamond composite bonded sample for different TEC stage temperatures at the same laser power density

Figure 54 shows the PL emission spectra from M262, without growth substrate removal, on a parylene-diamond composite bonded sample for different TEC stage temperatures

at the same laser power density. The Gaussian fitted PL emission peak energy versus heat sink temperature is plotted in Figure 55.

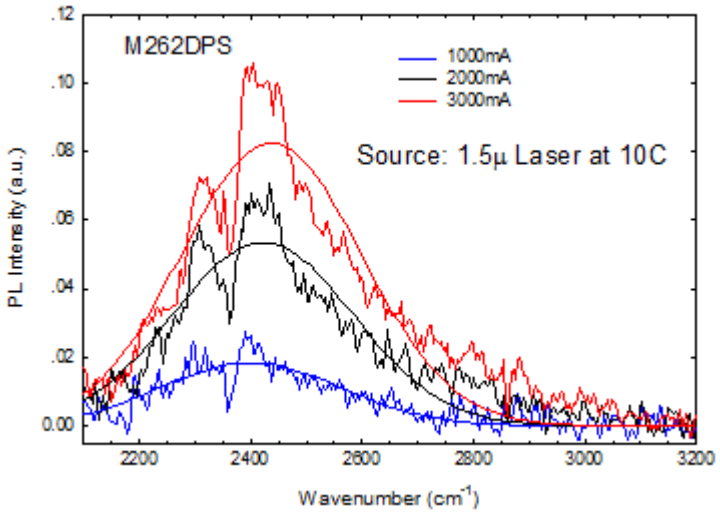

Figure 56: PL emission spectra from M262, without growth substrate removal on a parylene-diamond composite bonded sample for different laser power densities at the same TEC stage temperature

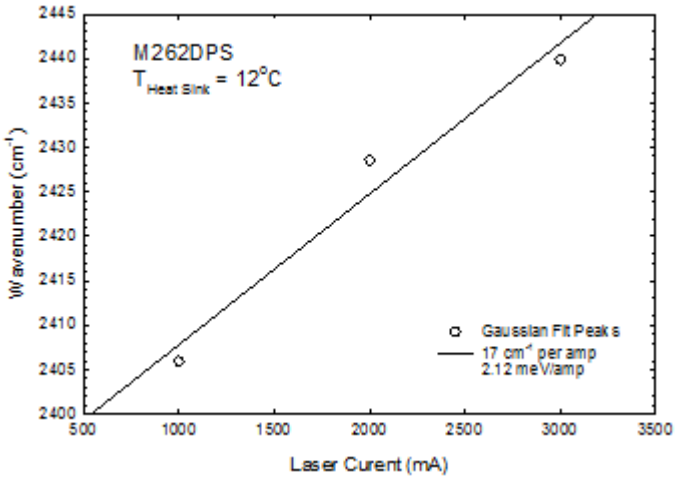

Figure 57: PL Peak energy from M262, without growth substrate removal, on a parylene-diamond composite bonded sample for different laser power densities at the same TEC stage temperature

Figure 57 shows PL emission spectra from M262, without growth substrate removal, on a parylene-diamond composite bonded sample for different laser power densities at the same TE stage temperature. The Gaussian fitted PL peak energy versus laser current is plotted in Figure 58. The slope of the linear regression fit is about 4.3 ℃ (17 cm^{-1}/A/3.95 cm^{-1}/℃) of heating per amp from 1A to 3A for the parylene-diamond composite bonded sample. These data clearly show that a parylene-diamond composite bond has the better heat dissipation than a parylene-only bond even if the concentration of diamond particles is low.

Figure 58 Slow dry chip with higher diamond water solution concentration

When the solution of diamond particles is increased, the quick dry method cannot get the uniform diamond layer deposition due to the tiny vibrations of the building and/or air flow. Therefore, the slow dry process in a desiccator with flat adjustable stage, like what is shown in Figure 59, was used to prepare samples with large diamond concentrations. Figure 58 is a photograph of a Si (100) chip with a high concentration of diamond particles after the slow drying is the desiccator.

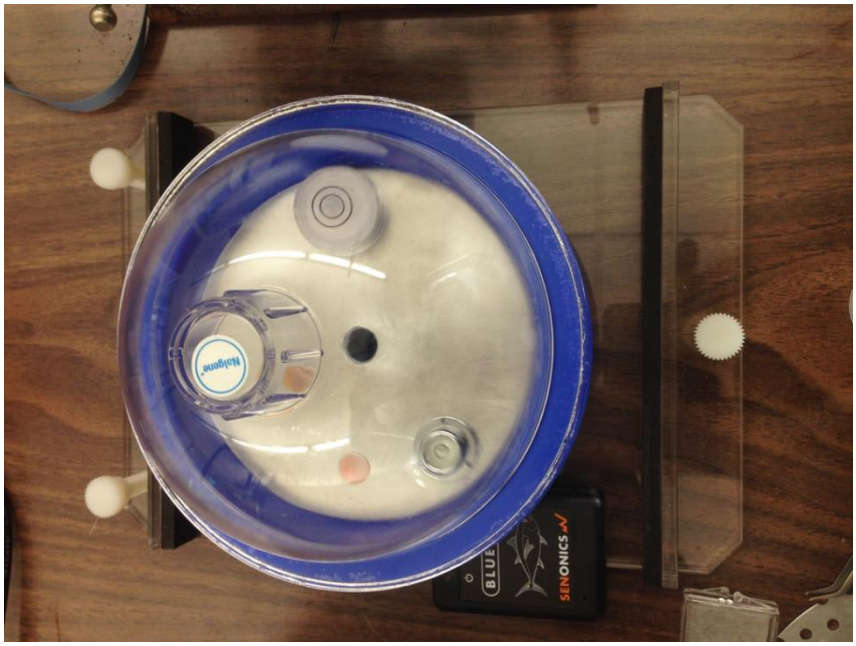

Figure 59 The desiccator with a flat plate for the slow dry process

The slow dry process takes at least a couple of hours. Figure 60 shows relative humidity data obtained with a Senonic Bluefin 1.0 sensor during slow drying at room temperature. The initial increase in relative humidity corresponds to establishment of a liquid-vapor equilibrium inside the desiccator. After about 4.7 hours the relative humidity rapidly decreases corresponding to complete removal of the source of the water vapor, which is the liquid on the chip.

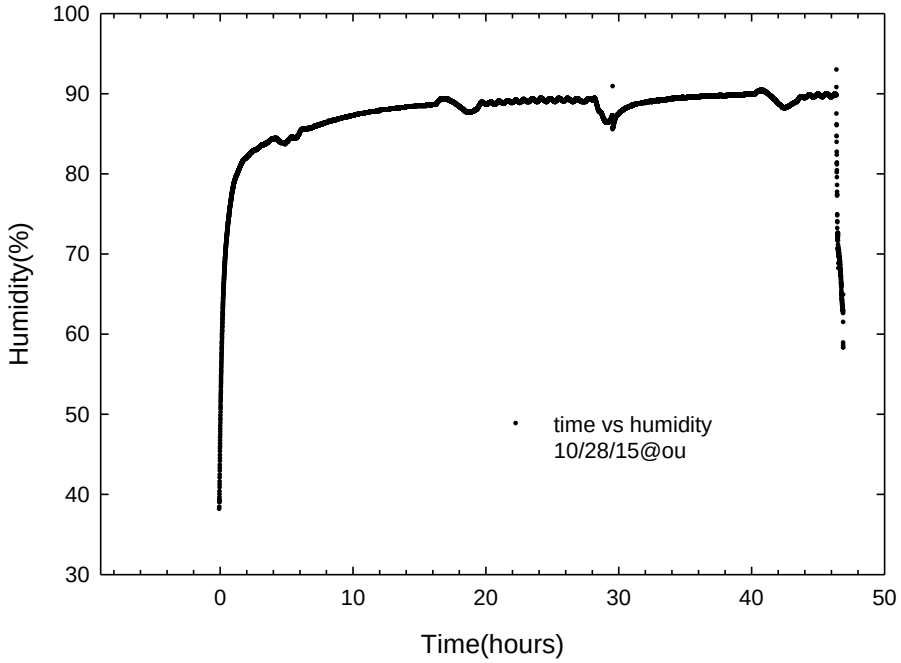

Figure 60 Humidity data during slow dry at room temperature

Si (100) chips with the high concentration diamond were coated with a parylene C thin film again then cleaned with DI water, methanol, acetone and an O_2 plasma for 10 seconds. After the cleaning, they were loaded parallel into the bonding chamber. After closing and sealing the chamber, the chamber pressure was reduced to 10^{-3} Torr. Bonding was accomplished with heating to 315℃ while ~1000g/cm^2 force was applied. Figure 61 and Figure 62 show the SEM images of the parylene-diamond composite bonding material. The parylene C appears to have melted during the bonding procedure.

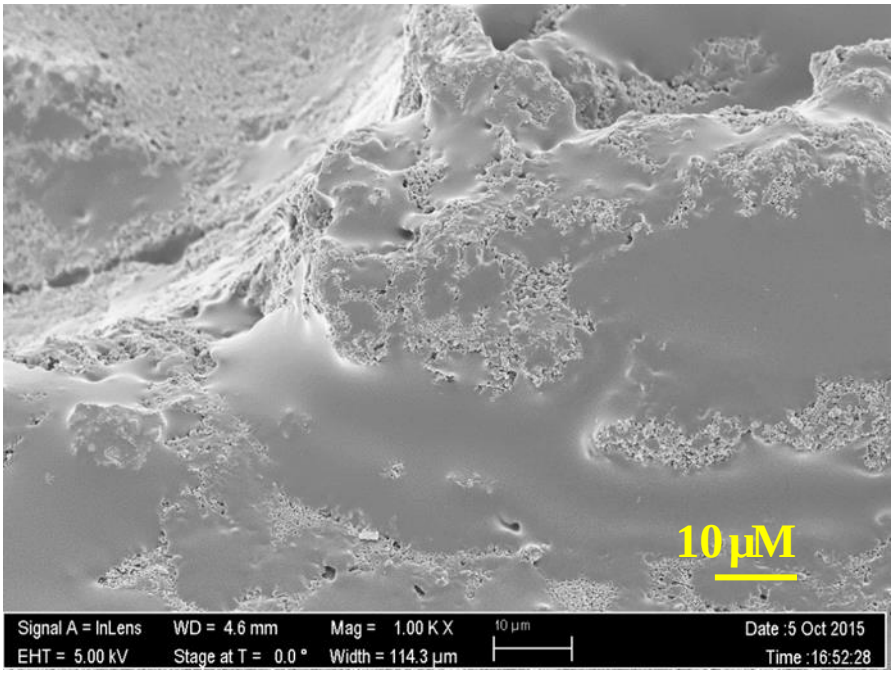

Figure 61 A SEM image of a high diamond concentration composite bonding material

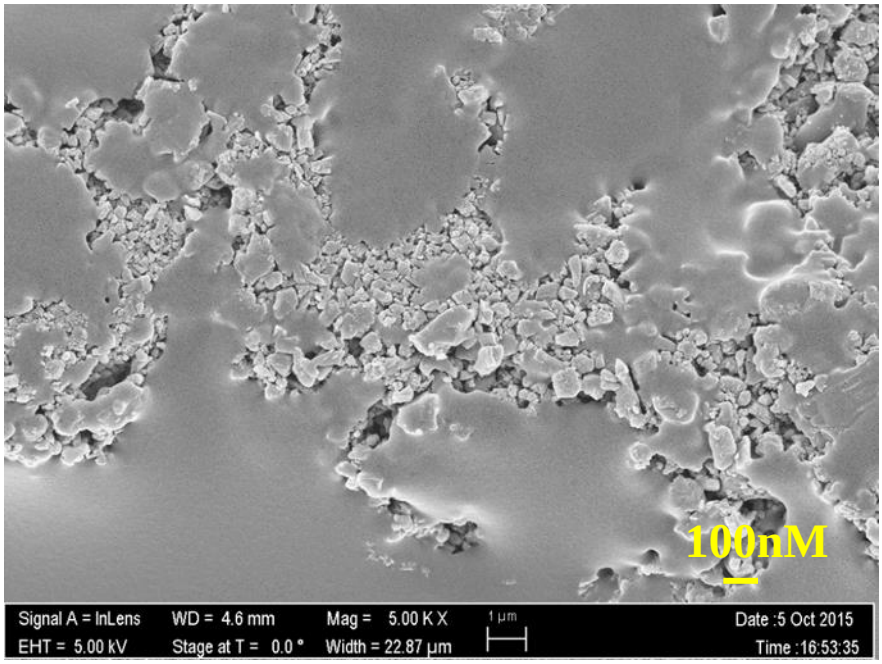

Figure 62 A SEM image of a high diamond concentration composite bonding material.

Double Side Polished Si Wafer Bonding

Double side polished low doped Si (100) wafers, purchased from University Wafer, with a thickness of 280 μm were cleaved and coated with a parylene-diamond-parylene sandwich as described above. Large diamond particles (0~2 μm) were used, so the thickness of parylene layer was more than 2 μm. Parylene-only coated chips were also prepared. The chips after all the depositions were cleaned with DI water, methanol, acetone and an O_2 plasma for 10 seconds. After the clean, they were loaded parallel into the bonding chamber, which was pumped down to 10^{-3} Torr. Bonding was accomplished with heater 300℃ and applying a force of ~4000g/cm^2.

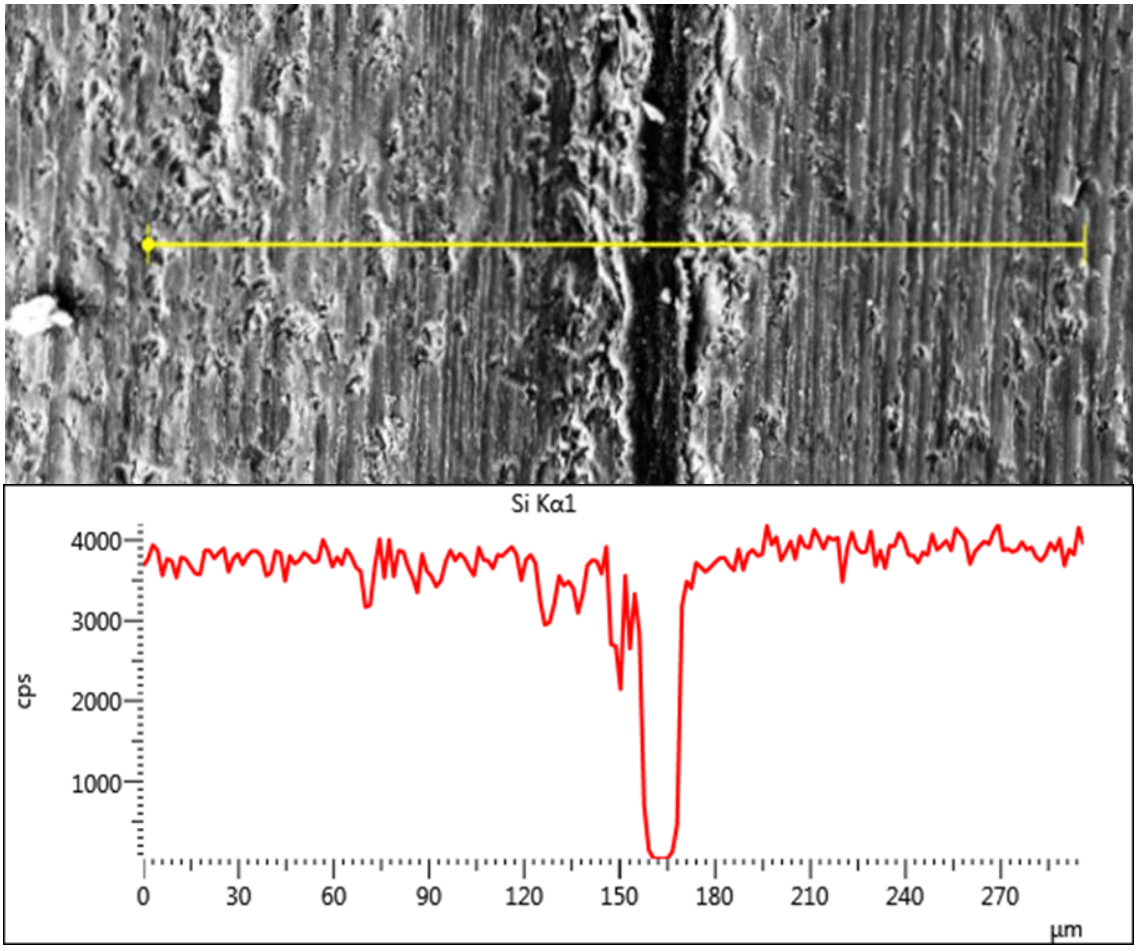

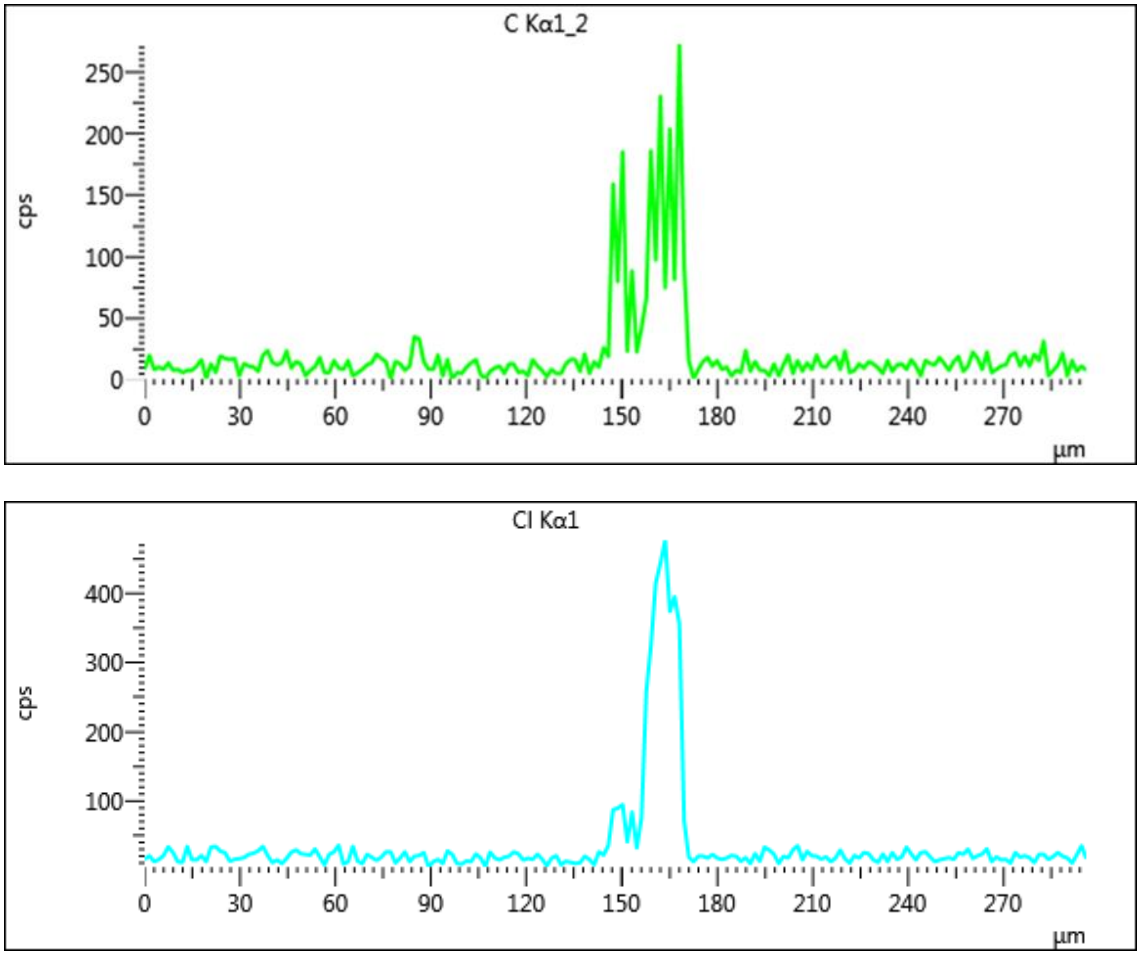

Figure 63 Cross section SEM image on the only parylene bonding sample and corresponding EDX scanning data

Figure 63 shows a cross sectional SEM image of the parylene-only bonded sample and corresponding EDX scanning data. Figure 64 shows a cross sectional SEM image of a parylene-diamond composite bonding material after O_2 plasma ashing for 15 minutes to selectively remove the parylene and its corresponding EDX scanning data. Because the chips were loaded in the same parylene deposition cycles, parylene-only and parylene-diamond composite substrates have almost the same bonding layer thickness (~10 µm). The EDX scanning data can prove this. During the wire saw cutting, the composite sample edge is not clear due to parylene migration to the edges.

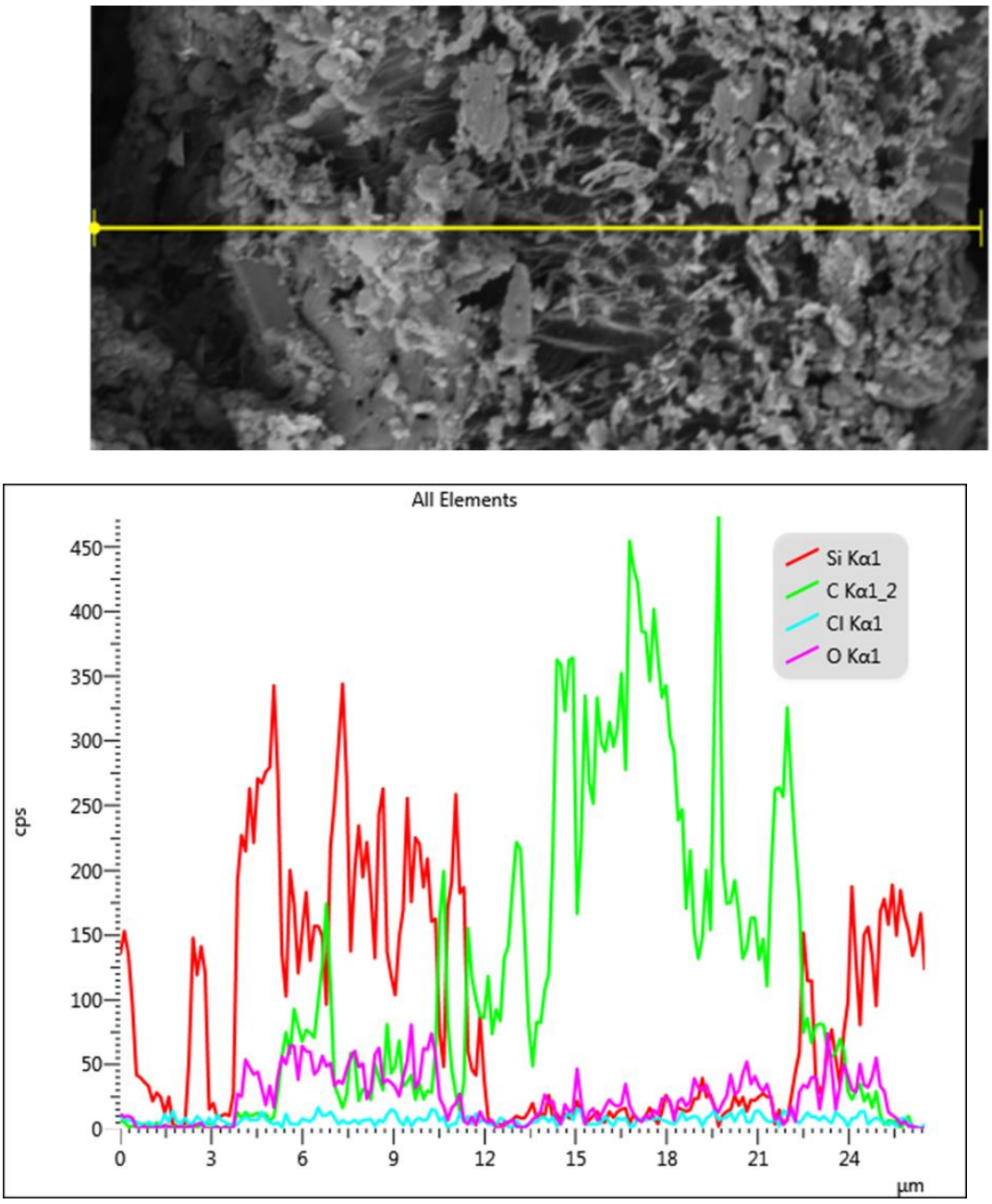

Figure 64 Cross section SEM image of a parylene-diamond composite bonding material after O_2 plasma ashing for 15 minutes and corresponding EDX scanning data

Eutectic Metal transfer bonding on the parylene/diamond bonded Si substrates

Eutectic metal transfer bonding technique [72,73] was applied to mounting the #M315 epi sample on the parylene/diamond bonded sandwich structure Si substrates. The bonding temperature is 130℃ and force set is ~8 (~1000g/cm^2).

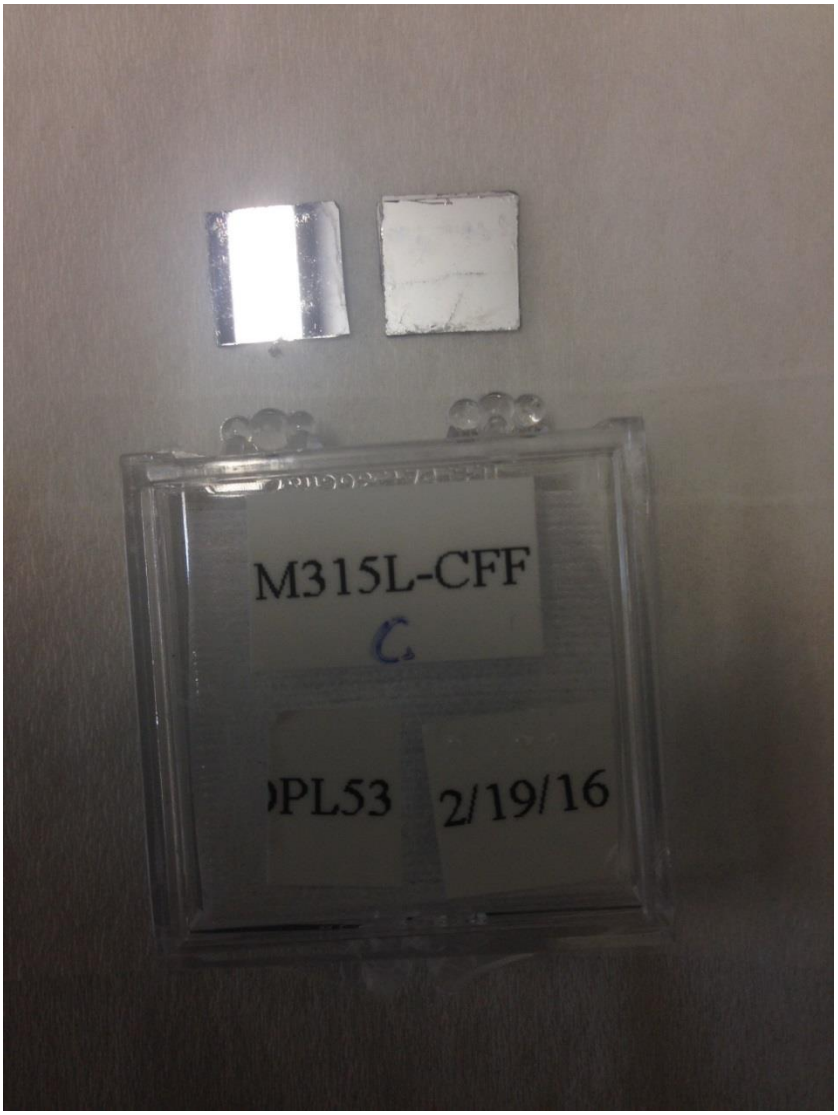

Figure 65 Image of M315 eutectic bonding to parylene-only bonded Si substrates after lift-off

Figure 66 Image of M315 eutectic bonded to parylene-diamond composite bonded Si substrates after M315 growth substrate lift-off

Figure 65 is an image of M315 after eutectic metal bonding to parylene-only bonded Si chips after MBE growth substrate lift-off, and Figure 66 is an image of M315 after eutectic metal bonding to parylene-diamond composite bonded Si chips after MBE growth substrate lift-off. DI water was used in the lift-off process. The lift-off process takes about 2 hours. After lift-off the samples were cleaned by HCl (5%).

Figure 67 shows PL emission spectra data from M315 on the parylene-only bonded sample form different TEC stage temperature at the same laser power density. Each PL emission spectrum was fitted with Gaussian function. The TEC stage setting

temperatures were set at 15℃, 20℃, 25℃, 30℃ and 35℃. Gaussian fitted PL peak energy versus heat sink temperature is plotted with a linear fit in Figure 68.

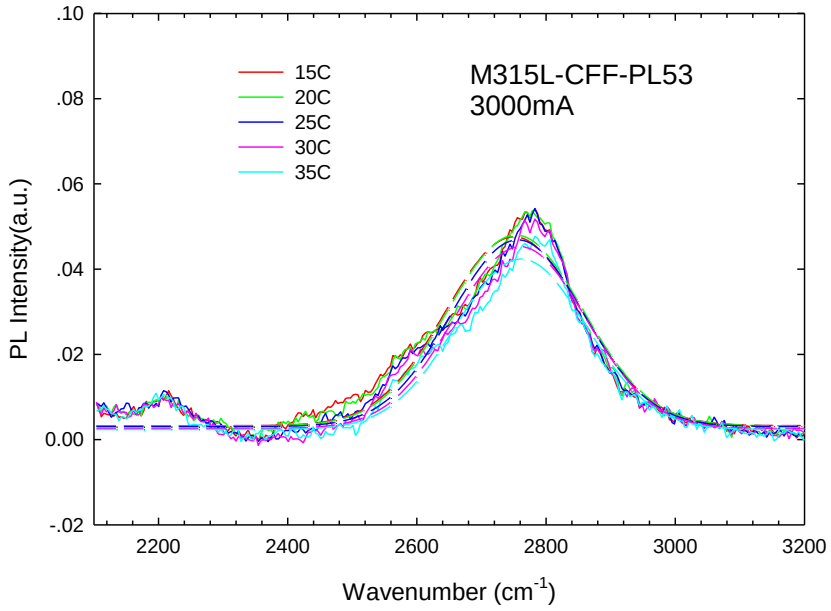

Figure 67: PL emission spectra on M315 lift-off parylene-only bonding sample when the different TE stage temperature was set at the same laser power density

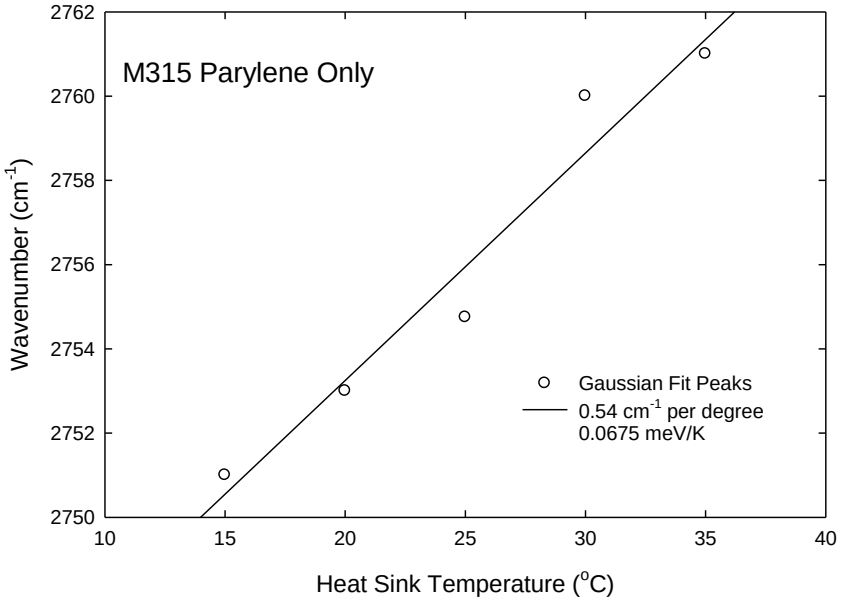

Figure68: PL peak energy versus heat sink temperature for M315 on a parylene-only bonded sample.

Figure 69 shows PL emission spectra from M315 on a parylene-only bonded sample for different laser power densities at the same TEC stage temperature. A clear blue shift in the PL peak energy is seen when the laser power density is increased as the laser current is increased from to 3000mA. Gaussian fitted PL peak energy versus laser current is plotted in Figure 70. The slope of the linear regression fitted line is 36.3℃ (19.6cm^{-1}/A/0.54cm^{-1}/℃) of heating per amp from 1A to 3A.

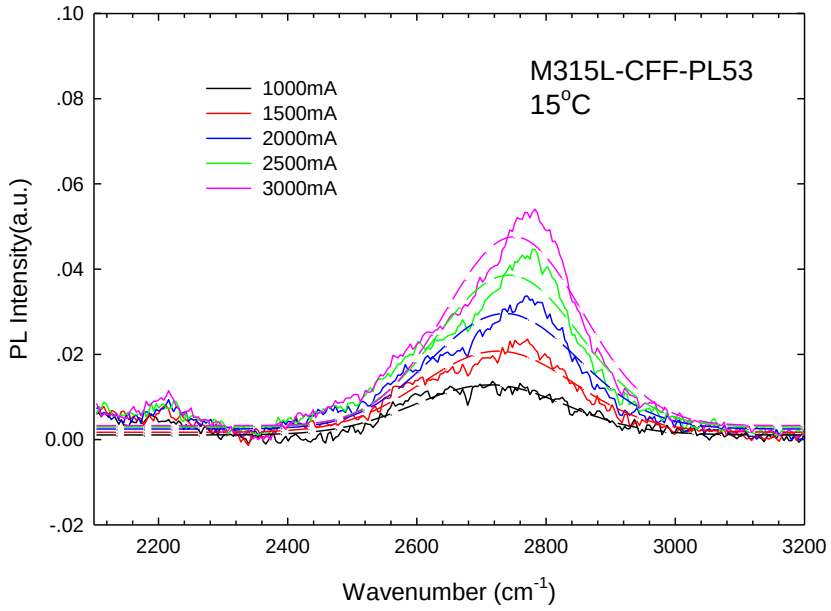

Figure 69: PL emission spectra from M315 lift-off parylene-only bonded sample for different laser power densities at the same TEC stage temperature

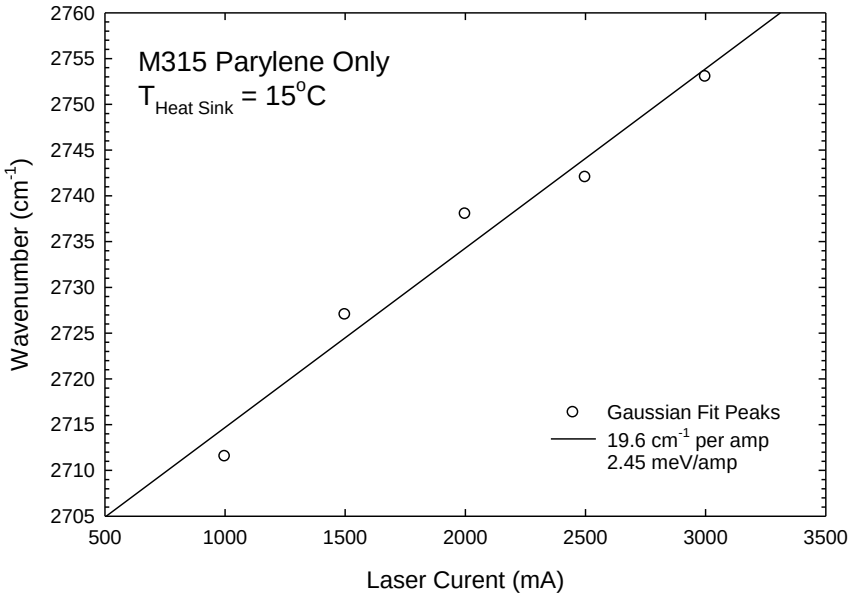

Figure 70: PL Peak energy versus laser current for M315 on parylene-only bonded sample

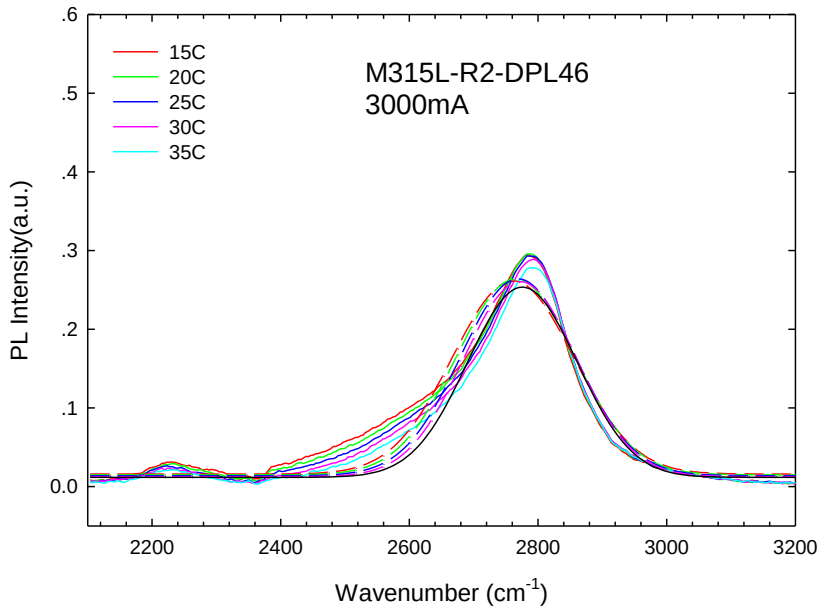

Figure 71: PL emission spectra from M315 lift-off parylene-diamond composite bonded sample for different TEC stage temperatures at the same laser power density

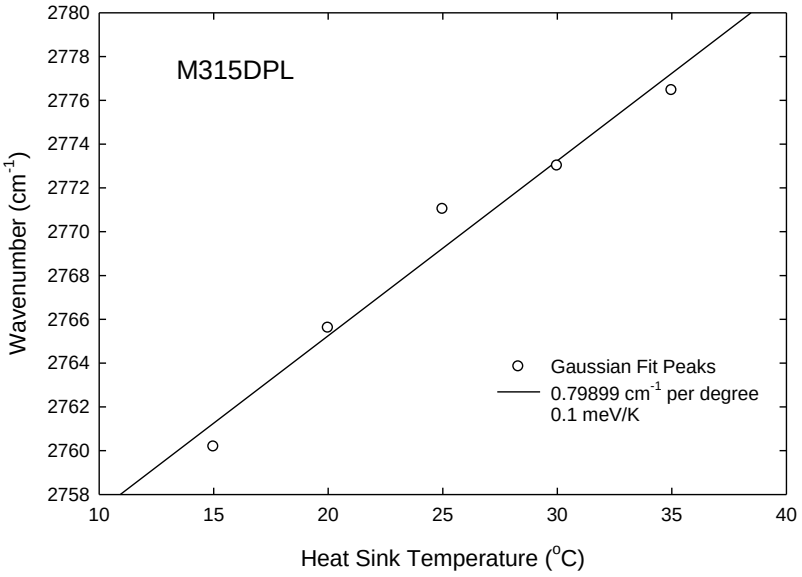

Figure 72: PL Peak energy versus heat sink temperature for M315 parylene-diamond composite bonded sample

Figure 71 shows PL emission spectra from M315 on a parylene-diamond composite bonded sample for different TEC stage temperatures at the same laser power density. Each PL emission spectrum was fitted with Gaussian function. The TE stage setting temperatures were set at 15℃, 20℃, 25℃, 30℃ and 35℃. Gaussian fitted PL peak energy versus heat sink temperature is plotted with a linear fit in Figure 72.

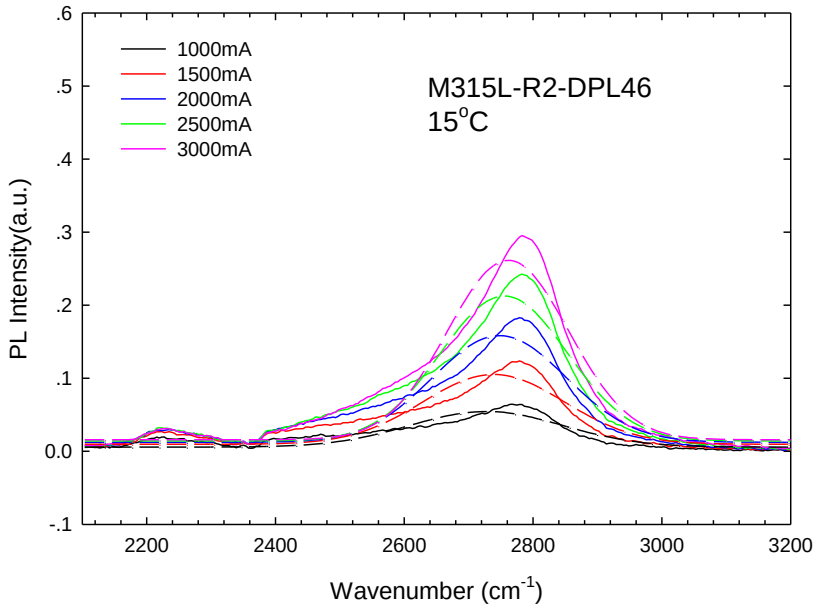

Figure 73: PL emission spectra from M315 lift-off parylene-diamond composite bonded sample for different laser power densities at the same TEC stage temperature

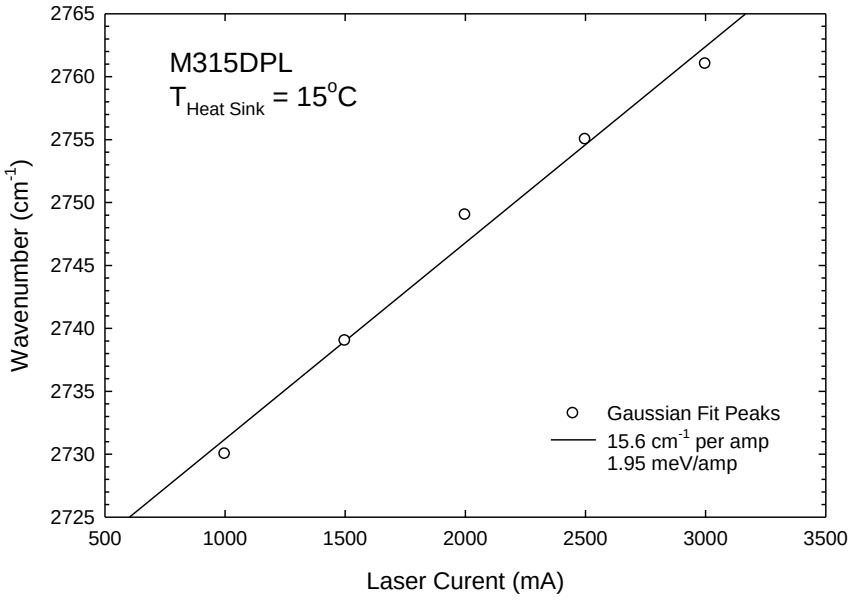

Figure 74: PL Peak energy versus laser current for M315 parylene-diamond composite bonded sample

Figure 73 shows PL emission spectra from M315 on a parylene-diamond bonded sample for different laser power densities at the same TEC stage temperature. A clear blue shift in the PL peak energy is seen when the laser power density is increased as the laser current is increased from 1000mA to 3000mA. Gaussian fitted PL peak energy verses laser current is plotted in Figure 74. The slope of the linear regression fitted line is 19.5℃ (15.6 cm^{-1}/A/0.8 cm^{-1}/℃) of heating per amp from 1A to 3A. Table 8 is the PL analysis data sheet.

Table 8 M315 PL data sheet

Sample:	**Temperature**	**PL peak(cm^{-1})**	**thermal conductivity**
315(Parylene)	15℃	2751	0.084 W/mK
	20℃	2753	
	25℃	2755	
	30℃	2760	
	35℃	2761	
M315(Composite)	15℃	2760	0.30 W/mK
	20℃	2765	
	25℃	2771	
	30℃	2773	
	35℃	2776	

Thermal Simulations on Parylene/Diamond Bonding Interface

Thin film thermal conductivity can be determined from the measured temperature increases associated with PL optical heating through thermal modeling. In this thesis finite element analysis (FEA) using a two-dimensional software package (Tera Analysis, Toronto, Canada model QuickField Ver. 5.6) was performed to extract the thin film thermal conductivity. Finite element thermal modeling was used to determine the thermal conductivity of the thin film material by using the hot spot temperatures obtained from the PL measurements as boundary

conditions.

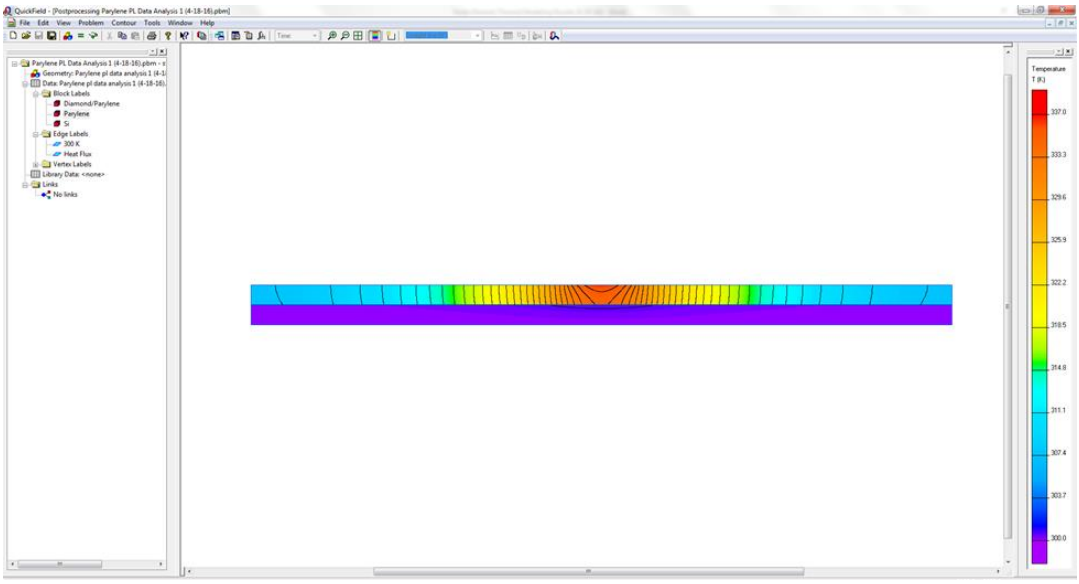

Figure 75 FEA thermal model results for M315 lift-off parylene-only bond sample

Figure 75 and Figure 76 show the FEA results as a color map with 1 ℃ isotherms indicating temperature (minimum: purple = 300K and maximum: 337K). The laser-induced hot spot was assumed to be 1 mm wide on the film surface, the thicknesses of Si (100) substrates was 280 μm and bonding layer thickness was 10 μm. The bulk thermal conductivity of parylene, which is 0.084 W/mK, gave 36.3 ℃ of heating when the hot spot power density was 134 W/cm^2, which is in good agreement with the estimated absorbed power density from the PL pump laser. The same 134 W/cm^2 hot spot power density was used to model the 19.5 ℃ of heating measured for the parylene-diamond composite bonded sample, and the fitted thermal conductivity of parylene-diamond composite material was found to be 0.30 W/mK.

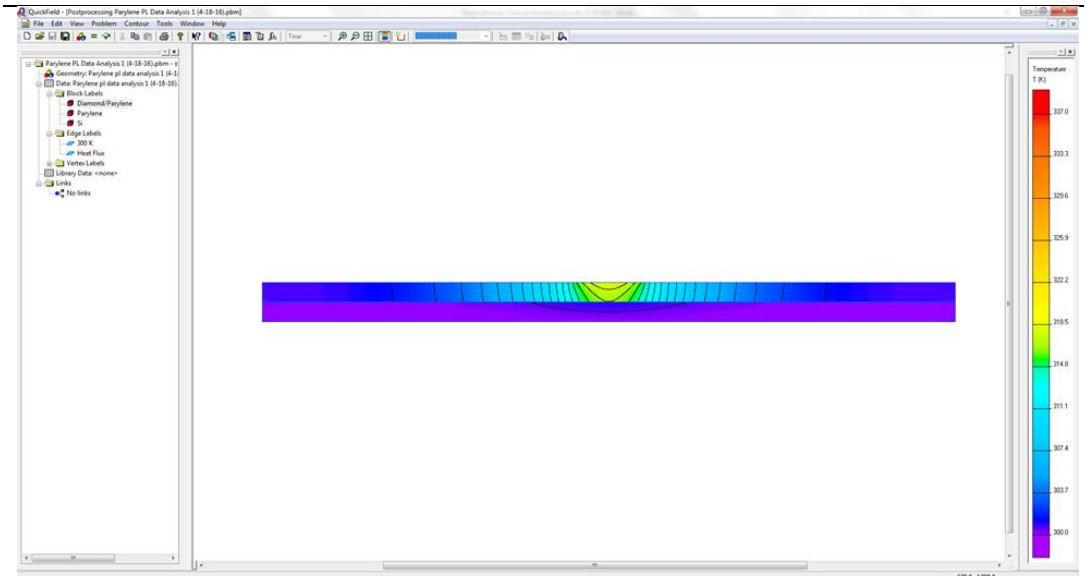

Figure 76 FEA thermal model results for M315 lift-off parylene-diamond composite bonded sample

Modeling results showed an improvement factor of 3.6 with incorporation of diamond. This corresponds to a thermal conductivity increase from 0.083 W/mK for bulk parylene to 0.30 W/mK for the parylene/diamond composite material.

Conclusion

The parylene-diamond composite bonded substrates have better heat dissipation even if the concentration of diamond particles is low. The amount of heating with a parylene/diamond composite bonding material was 19.5℃, which was significantly lower than the 36.3℃ observed for a control sample that was parylene bonded without diamond. These data show that incorporation of diamond particles in parylene can significantly reduce hot spot temperatures in electronic devices. Finite element thermal modeling was used to determine the thermal conductivity of the parylene/diamond composite material using the hot spot temperatures obtained from the PL measurements

as boundary conditions. Modeling results showed an improvement of 3.6x with incorporation of diamond. This corresponds to a thermal conductivity increase from 0.083 W/mK for bulk parylene to 0.30 W/mK for the parylene/diamond composite material. Furthermore, the ability to form a thin bond with a thickness of 10 μm or less provides additional thermal management benefits over other device packaging techniques that involve much thicker bonding layers. A proof-of-concept has thus been established for the opportunity to develop an improved electronic device packaging material based on thin film parylene/diamond composites. In addition, this thesis has shown that thermal conductivities of experimental thin film materials for thermal management applications can be obtained by using photoluminescence measurements of IV-VI semiconductor thin films to determine the boundary conditions for finite element thermal modeling analysis.

This analysis method can be used in future work to develop improved thin film interface material for packaging electronic components such as, high-power transistors, semiconductor lasers, and computer processors. The future applications are shown in Figure 76. Besides electronics and computer applications, it can also be applied in medical, transportation, energy, aerospace, and defense applications demanding high-heat-flux cooling schemes

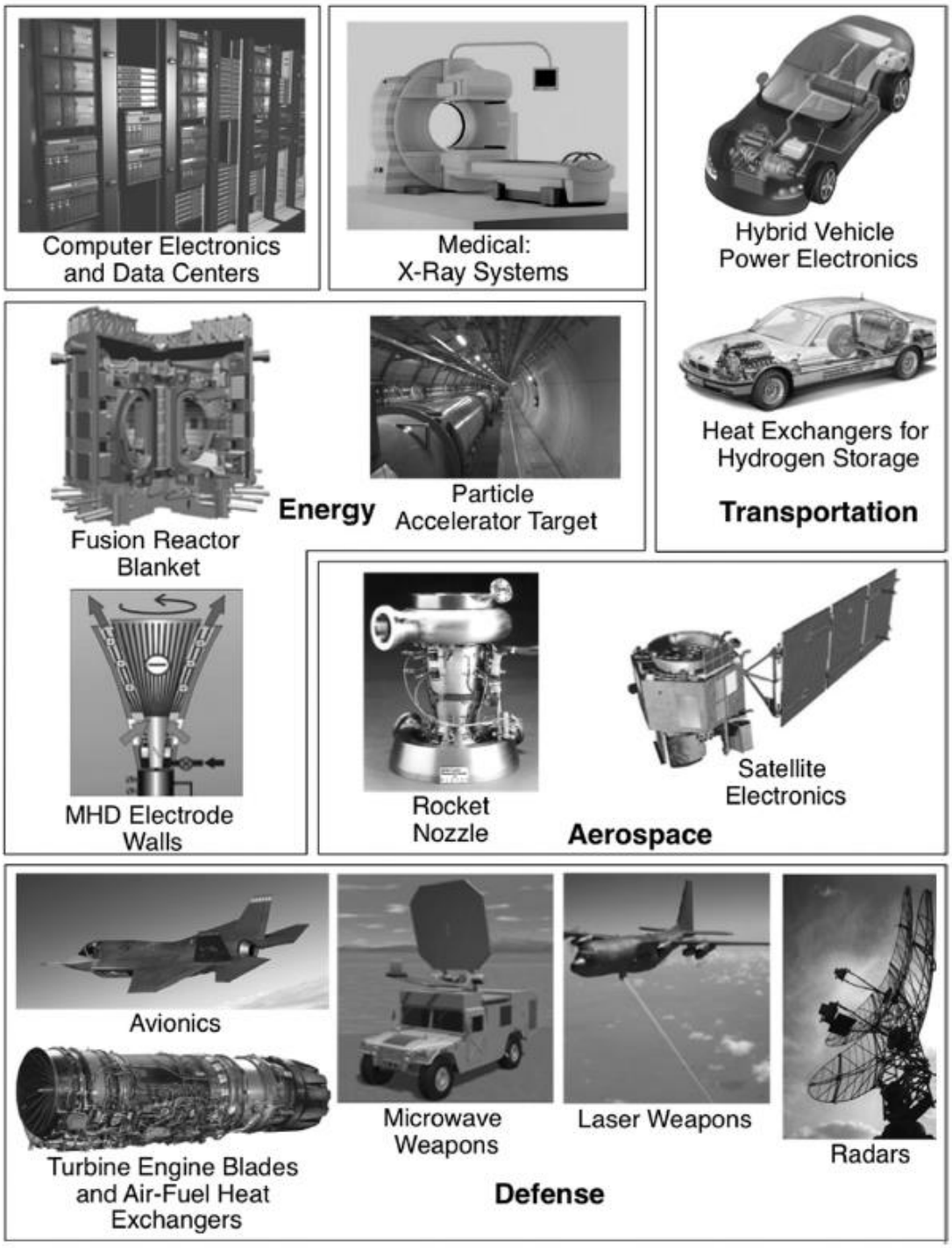

Figure 77 Examples of computer, medical, transportation, energy, aerospace, and defense applications demanding high-heat-flux cooling schemes [12]

Chapter 4: Summary & Future work

In this thesis, a new composite bonding material for improving the thermal management of packaged high power electronic devices and a method for measuring its thermal conductivity were described. Continued improvements in this new material are possible, and this will lead to better solid state electronic device performance and reliability. IV-VI semiconductor epitaxial material, which is grown by MBE, was used to measure hot spot temperatures thus providing the boundary conditions to determine the thermal conductivity of the thin film bonding interface material. After composite parylene bonding and eutectic metal bonding, SEM and EDX measurements showed a good and uniform bonding medium. Like other thermal conductivity measurements, a thermal model simulation based on the PL analysis is needed for thermal analysis.

Chapter 1 described the background and motivation on this research. Chapter 2 described measurements of electrical Hall effect and optical properties for different IV-VI materials. Chapter 3 described a novel, non-contact optical characterization technique to measure the surface temperature of heated parylene-only and the parylene-diamond composite bonded samples. This work included measuring PL spectra from IV-VI semiconductor material at heat sink temperatures from 15℃ to 35℃ with different amounts of incident optical power. Finite element thermal modeling was used to calculate thermal conductivity from the temperature increase data for the different materials tested.

Future improvements to the process of fabrication and packaging of high power devices can involve:

1. Optimizing the solution to make more diamond particles deposited. If so, higher thermal conductivity composite material can be produced.
2. Mixing large and small diamond particles and optimizing the mixture ratio. This can maximize the diamond volume ratio in the composites. Better heat dissipation properties can be found.
3. Replacing the two double polished Si chips with polished copper chips. The PL on those substrates will have better fit results and better total heat dissipation capability on the devices.
4. Keeping a horizontal level during the slow dry process in the desiccator.
5. Improving the processing steps to get the ultra-flat and clean surfaces prior to bonding.
6. Instead of diamond particles, BAs, BN, BP or graphene can be filled in the polymer material to increase thermal conductivity.

References

1. J. Schleeh, J. Mateos, I. Iniguez-de-la-Torre, N. Wadefalk, P. A. Nilsson, J. Grahn, and A. J. Minnich, "Phonon black-body radiation limit for heat dissipation in electronics," Nature materials **14** (2), 187-192 (2015).

2. Jungwan Cho and Kenneth E Goodson, "Thermal transport: cool electronics," Nature materials **14** (2), 136-137 (2015).

3. Jungwan Cho, Zijian Li, Mehdi Asheghi, and Kenneth E Goodson, "Near-junction thermal management: Thermal conduction in gallium nitride composite substrates," Ann. Rev. Heat Transfer **18** (2014).

4. Ihtesham Chowdhury, Ravi Prasher, Kelly Lofgreen, Gregory Chrysler, Sridhar Narasimhan, Ravi Mahajan, David Koester, Randall Alley, and Rama Venkatasubramanian, "On-chip cooling by superlattice-based thin-film thermoelectrics," Nature Nanotechnology **4** (4), 235-238 (2009).

5. Philip Ball, "Computer engineering: Feeling the heat," Nature **492** (7428), 174-176 (2012).

6. Roman M Katchmar, "Method and device for heat dissipation in an electronics system", (Patents, 2002).

7. Zhonghao Rao and Shuangfeng Wang, "A review of power battery thermal energy management," Renewable and Sustainable Energy Reviews **15** (9), 4554-4571 (2011).

8. Darrel Eugene Peugh, Joanna Christine Berndt, and Bruce Alan Myers, "Flip chip on circuit board with enhanced heat dissipation and method therefor", (Patents, 2000).

9. Xingcun Colin Tong, *Advanced materials for thermal management of electronic packaging*. (Springer Science & Business Media, 2011).

10. Carl Zweben, "Advances in composite materials for thermal management in electronic packaging," Jom **50** (6), 47-51 (1998).

11. Sergey V Kidalov and Fedor M Shakhov, "Thermal conductivity of diamond composites," Materials **2** (4), 2467-2495 (2009).

12. Mudawar, Issam. "Recent advances in high-flux, two-phase thermal management." Journal of Thermal Science and Engineering Applications **5** (2013): 021012.

13. Young, R. "Developments and trends in thermal management technologies–a

mission to the USA." (2010).

14. Tianli Feng and Xiulin Ruan, "Prediction of spectral phonon mean free path and thermal conductivity with applications to thermoelectrics and thermal management: a review," Journal of Nanomaterials **2014** (2014).

15. PG Klemens, "Thermal conductivity and lattice vibrational modes," Solid state physics **7**, 1-98 (1958).

16. AA Maradudin and AE Fein, "Scattering of neutrons by an anharmonic crystal," Physical Review **128** (6), 2589 (1962).

17. AA Maradudin, AE Fein, and GH Vineyard, "On the evaluation of phonon widths and shifts," physica status solidi (b) **2** (11), 1479-1492 (1962).

18. Wu Li, Natalio Mingo, Lucas Lindsay, David A Broido, Derek A Stewart, and Nebil A Katcho, "Thermal conductivity of diamond nanowires from first principles," Physical Review B **85** (19), 195436 (2012).

19. DPH Hasselman and Lloyd F Johnson, "Effective thermal conductivity of composites with interfacial thermal barrier resistance," Journal of Composite Materials **21** (6), 508-515 (1987).

20. Geon-Woong Lee, Min Park, Junkyung Kim, Jae Ik Lee, and Ho Gyu Yoon, "Enhanced thermal conductivity of polymer composites filled with hybrid filler," Composites Part A: Applied Science and Manufacturing **37** (5), 727-734 (2006).

21. Reza Tavangar, Jose Miguel Molina, and Ludger Weber, "Assessing predictive schemes for thermal conductivity against diamond-reinforced silver matrix composites at intermediate phase contrast," Scripta Materialia **56** (5), 357-360 (2007).

22. David G Cahill, Henry E Fischer, Tom Klitsner, ET Swartz, and RO Pohl, "Thermal conductivity of thin films: measurements and understanding," Journal of Vacuum Science & Technology A **7** (3), 1259-1266 (1989).

23. David G Cahill, "Thermal conductivity measurement from 30 to 750 K: the 3ω method," Review of scientific instruments **61** (2), 802-808 (1990).

24. S Lee, David G Cahill, and Rama Venkatasubramanian, "Thermal conductivity of Si-Ge superlattices," Applied physics letters **70** (22) (1997).

25. T Borca-Tasciuc, AR Kumar, and G Chen, "Data reduction in 3ω method for thin-film thermal conductivity determination," Review of scientific instruments **72** (4), 2139-2147 (2001).

26. CE Raudzis, F Schatz, and D Wharam, "Extending the 3ω method for thin-film analysis to high frequencies," Journal of applied physics **93** (10), 6050-6055 (2003).

27. RJ Stoner and HJ Maris, "Kapitza conductance and heat flow between solids at temperatures from 50 to 300 K," Physical Review B **48** (22), 16373 (1993).

28. Jie Zhu, Dawei Tang, Wei Wang, Jun Liu, Kristopher W Holub, and Ronggui Yang, "Ultrafast thermoreflectance techniques for measuring thermal conductivity and interface thermal conductance of thin films," Journal of Applied Physics **108** (9), 094315 (2010).

29. John C Lambropoulos, MR Jolly, CA Amsden, SE Gilman, MJ Sinicropi, D Diakomihalis, and SD Jacobs, "Thermal conductivity of dielectric thin films," Journal of applied physics **66** (9), 4230-4242 (1989).

30. AJ Griffin Jr, FR Brotzen, and PJ Loos, "The effective transverse thermal conductivity of amorphous Si3N4 thin films," Journal of applied physics **76** (7), 4007-4011 (1994).

31. Stéphane Orain, Yves Scudeller, and Thierry Brousse, "Structural and microstructural effects on the thermal conductivity of zirconia thin films," Microscale Thermophysical Engineering **5** (4), 267-275 (2001).

32. M Okuda and S Ohkubo, "A novel method for measuring the thermal conductivity of submicrometre thick dielectric films," Thin Solid Films **213** (2), 176-181 (1992).

33. S Ohkubo and M Okuda, "A method for the determination of the thermal transport properties of submicron-thick dielectric films with the use of an analytical expression," Thin solid films **219** (1), 239-243 (1992).

34. PL Woodfield, J Fukai, M Fujii, Y Takata, and K Shinzato, "A two-dimensional analytical solution for the transient short-hot-wire method," International Journal of Thermophysics **29** (4), 1278-1298 (2008).

35. S Min Lee and David G Cahill, "Heat transport in thin dielectric films," Journal of applied physics **81** (6), 2590-2595 (1997).

36. Yee Kan Koh, Suzanne L Singer, Woochul Kim, Joshua MO Zide, Hong Lu, David G Cahill, Arun Majumdar, and Arthur C Gossard, "Comparison of the 3w method and time-domain thermoreflectance for measurements of the cross-plane thermal conductivity of epitaxial semiconductors," Journal of Applied Physics **105** (5), 54303 (2009).

37. David G Cahill and Robert O Pohl, "Thermal conductivity of amorphous solids above the plateau," Physical review B **35** (8), 4067 (1987).

38. David G Cahill, Wayne K Ford, Kenneth E Goodson, Gerald D Mahan, Arun Majumdar, Humphrey J Maris, Roberto Merlin, and Simon R Phillpot, "Nanoscale thermal transport," Journal of Applied Physics **93** (2), 793-818 (2003).

39. Aaron J Schmidt, Xiaoyuan Chen, and Gang Chen, "Pulse accumulation, radial heat conduction, and anisotropic thermal conductivity in pump-probe transient thermoreflectance," Review of Scientific Instruments **79** (11), 114902 (2008).

40. William S Capinski and Humphrey J Maris, "Improved apparatus for picosecond pump–and–probe optical measurements," Review of Scientific Instruments **67** (8), 2720-2726 (1996).

41. Keith T Regner, Daniel P Sellan, Zonghui Su, Cristina H Amon, Alan JH McGaughey, and Jonathan A Malen, "Broadband phonon mean free path contributions to thermal conductivity measured using frequency domain thermoreflectance," Nature communications **4**, 1640 (2013).

42. Patrick J McCann, Leonard Olona, Zhihua Cai, James D Jeffers, and Khosrow Namjou, presented at the MRS Proceedings (2012).

43. James D Jeffers, Khosrow Namjou, Zhihua Cai, Patrick J McCann, and Leonard Olona, "Cross-plane thermal conductivity of a PbSnSe/PbSe superlattice material," Applied Physics Letters **99** (4), 041903 (2011).

44. James Dominic Jeffers, *Thermal conductivity measurements of IV-VI semiconductor nanostructures*. (THE UNIVERSITY OF OKLAHOMA, 2013).

45. Nam-Ho Kim, "Finite elements for heat transfer problems,"

46. PDS 2010 LABCOTER 2 Parylene Depositon System Operator's Manual

47. Hanseup Kim and Khalil Najafi, "Characterization of low-temperature wafer bonding using thin-film parylene," Microelectromechanical Systems, Journal of **14** (6), 1347-1355 (2005).

48. Manijeh Razeghi, *Fundamentals of solid state engineering*. (Springer Science & Business Media, 2009).

49. Gaspe Mudiyanselage and K Chomani, *Molecular beam epitaxy of narrow gap quantum wells: Indium antimonide, Indium-gallium-arsenic and elemental antimony*. (2013).

50. Patrick J McCann and Dongfan Zhong, "Liquid phase epitaxy growth of Pb1− xSnxSe1− yTey alloys lattice matched with BaF2," Journal of applied physics **75** (2), 1145-1150 (1994).

51. HK Sachar, I Chao, PJ McCann, and XM Fang, "Growth and characterization of PbSe and Pb1− xSnxSe on Si (100)," Journal of applied physics **85** (10), 7398-7403 (1999).

52. John Androulakis, Duck-Young Chung, Xianli Su, Li Zhang, Ctirad Uher, Thomas C Hasapis, Euripides Hatzikraniotis, Konstantinos M Paraskevopoulos, and Mercouri G Kanatzidis, "High-temperature charge and thermal transport properties of the n-type thermoelectric material PbSe," Physical Review B **84** (15), 155207 (2011).

53. John Androulakis, Chia-Her Lin, Hun-Jin Kong, Ctirad Uher, Chun-I Wu, Timothy Hogan, Bruce A Cook, Thierry Caillat, Konstantinos M Paraskevopoulos, and Mercouri G Kanatzidis, "Spinodal decomposition and nucleation and growth as a means to bulk nanostructured thermoelectrics: Enhanced performance in Pb1-x Sn x Te-PbS," Journal of the American Chemical Society **129** (31), 9780-9788 (2007).

54. Bo Zhang, Jian He, and Terry M Tritt, "Size-selective high-yield growth of lead telluride (PbTe) nanocrystals using a chemical vapor deposition technique," Applied physics letters **88** (4), 043119 (2006).

55. Lee Andrew Elizondo, *Low-dimensional IV-VI semiconductor materials*. (THE UNIVERSITY OF OKLAHOMA, 2008).

56. Patrick J McCann, I-Na Chao, Harpreet Sachar, Denton McAlister, Chun-Pang Li, Xiao-Ming Fang, Huizhen Wu, and Khosrow Namjou, "IV–VI Semiconductor growth on silicon substrates and new mid-infrared laser fabrication methods," Spectrochimica Acta Part A: Molecular and Biomolecular Spectroscopy **55** (10) (1999).

57. Brian R Pamplin, *Molecular beam epitaxy*. (Elsevier, 2013).

58. Dmitriy Khokhlov, *Lead chalcogenides: physics and applications*. (CRC Press, 2002).

59. P Müller, A Fach, J John, AN Tiwari, H Zogg, and G Kostorz, "Structure of epitaxial PbSe grown on Si (111) and Si (100) without a fluoride buffer layer," Journal of applied physics **79** (4), 1911-1916 (1996).

60. H Zogg and M Hüppi, "Growth of high quality epitaxial PbSe onto Si using a (Ca, Ba) F2 buffer layer," Applied Physics Letters **47** (2), 133-135 (1985).

61. H Zogg, P Müller, A Fach, J John, C Paglino, and S Teodoropol, presented at the MRS Proceedings, 1995

62. https://en.wikipedia.org/wiki/Hall_effect.

63. Safa Kasap, *Hall effect in semiconductors*. (Web-Materials, 2001).

64. PHILIPS'GLOEILAMPENFABRIEKEN, "A method of measuring specific resistivity and Hall effect of discs of arbitrary shape," Philips Research Reports **13** (1) (1958).

65. Neil W Ashcroft and N David Mermin, "Solid state physics," (1976).

66. Gunther Springholz and Günther Bauer, "Semiconductors, IV–VI," Wiley Encyclopedia of Electrical and Electronics Engineering (1999).

67. Sangeetha Vijeyaragunathan, *Investigation into molecular beam epitaxial growth and characterization of InGaAs structures and InAs superlattices* UNIVERSITY OF OKLAHOMA, 2014.

68. Thomas R Harris, *Optical properties of Si, Ge, GaAs, GaSb, InAs, and InP at elevated temperatures*, 2010.

69. WZ Shen, K Wang, LF Jiang, XG Wang, SC Shen, HZ Wu, and PJ McCann, "Study of band structure in PbSe/PbSrSe quantum wells for midinfrared laser applications," Applied Physics Letters **79** (16), 2579-2581 (2001).

70. Hanseup Kim and Khalil Najafi, "Characterization of low-temperature wafer bonding using thin-film parylene," Microelectromechanical Systems, Journal of **14** (6), 1347-1355 (2005).

71. https://en.wikipedia.org/wiki/Parylene

72. Y. F. Li, A. Sow, C. Yao and P. J. McCann, "Transfer of IV-VI Multiple Quantum Well Structures Grown by Molecular Beam Epitaxy from Si Substrates to Copper", *Thin Solid Films* **488**, 178 (2005).

73. Y. F. Li, P. J. McCann, A. Sow, C. Yao, and P. C. Kamat, "Improvement of Heat Dissipation Through Transfer of IV-VI Epilayers From Silicon to Copper", *IEEE Photonics Technology Letters* **16**, 2433 (2004).

74. http://www.microchemicals.com/products/wafers/wafer_specification.html

75. http://www.pveducation.org/pvcdrom/materials/optical-properties-of-silicon

76. M Balkanski, A Aziza, and E Amzallag, "Infrared Absorption in Heavily Doped n - Type Si," physica status solidi (b) **31** (1), 323-330 (1969).

Appendix A: Parylene Deposition Data Sheet

Mass of Parylene C(g)	Thickness (μm)
1.7262	1.05
3.5540	2.17
3.5797	2.2
4.0892	2.47
4.1723	2.53

Appendix B: Optical Image on Diamond Particle Deposition

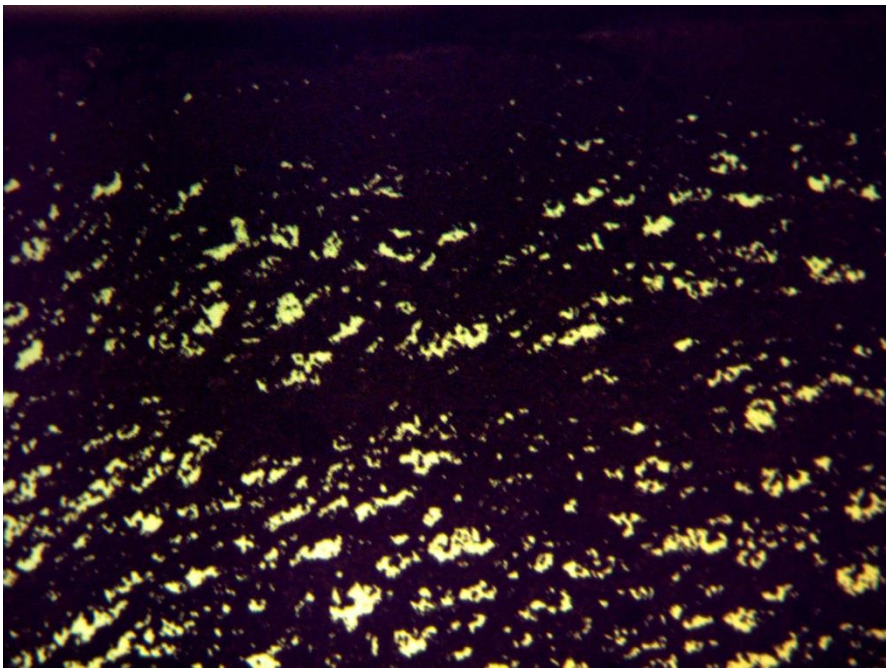

DPL32-2-10-15

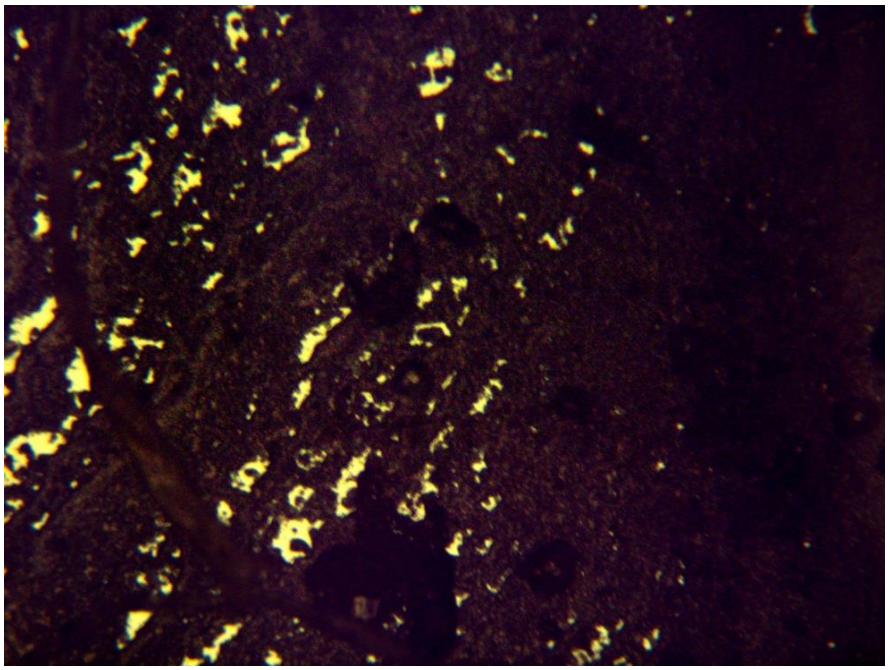

DPL32-2-10-15 in 100 μm scale

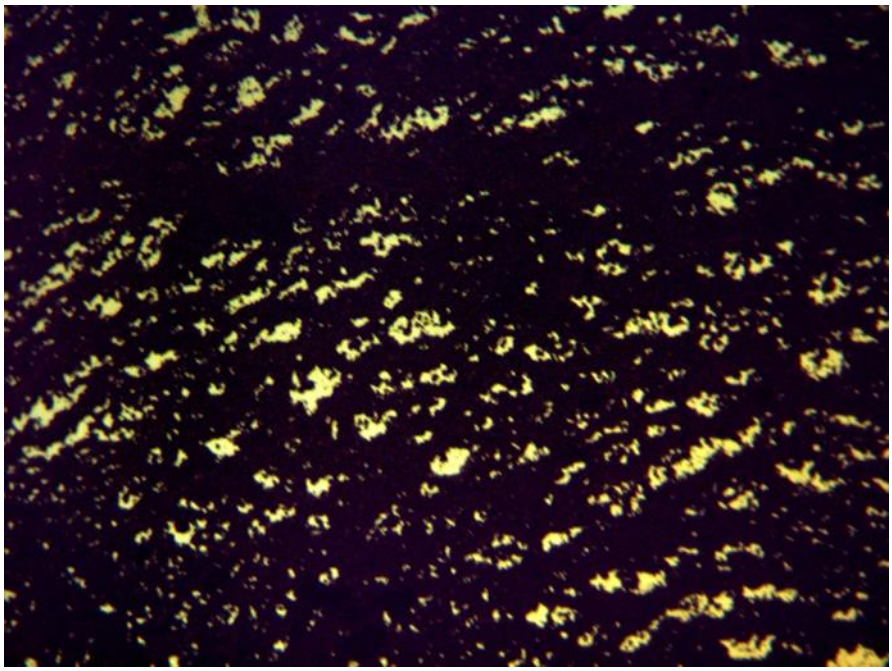

DPL32-2-10-15 in 200μm scale

Appendix C: Structure on the M315 bonding sample

Si (111)
Buffer
Epi layer
Eutectic Metal
Si (100)
Parylene/Diamond
Si (100)